White, D. J. & Bolton, M. D. (2004). *Géotechnique* **54**, No. 6, 375–397

Displacement and strain paths during plane-strain model pile installation in sand

D. J. WHITE* and M. D. BOLTON*

The underlying mechanisms governing the behaviour of displacement piles in sand are not well understood, leading to unreliability in design methods. A series of plane-strain calibration chamber tests has been conducted in order to quantify the penetration mechanism around the pile tip, and the response of the interface layer adjacent to the shaft during further penetration. A series of eight tests is reported, examining the influence of soil type, initial state, pile breadth and the use of a driving shoe. A novel image-based deformation measurement technique has been used to observe the displacement and strain paths, which are found to be relatively independent of soil type. The measured strain paths are similar to predictions made by the strain path method, and contrast sharply with assumptions implicit in cavity expansion solutions. An interface zone adjacent to the pile shaft comprising fine broken soil particles was observed to contract while shearing along the pile–soil interface. This mechanism offers an explanation for the degradation of shaft friction at a given soil horizon with increased pile penetration ('friction fatigue'), and a subsequent recovery of capacity over time ('set-up').

KEYWORDS: bearing capacity; calcareous soils; friction; model tests; piles; sands

Les mécanismes sous-jacents gouvernant le comportement de piles de déplacement dans du sable ne sont pas bien compris, ce qui nuit à la fiabilité des méthodes de conception. Nous avons effectué une série d'essais de plan-déformation en chambres de calibrage afin de quantifier le mécanisme de pénétration autour des extrémités de piles ainsi que la réponse de la zone interface adjacente au tronc pendant la pénétration consécutive. Nous rapportons les résultats d'une série de huit tests, examinant l'influence du type de sol, l'état initial, la largeur de la pile et l'utilisation d'un sabot moteur. Nous utilisons une nouvelle technique à imagerie pour mesurer la déformation et pour observer les chemins de déplacement et de déformation qui se sont révélés être relativement indépendants du type de sol. Les chemins de déformation mesurés sont similaires aux prévisions faites par la méthode de chemin de déformation et contrastent nettement avec les suppositions implicites dans les solutions d'expansion de cavité. Nous avons constaté qu'une zone interface adjacente au tronc de la pile et constituée de fines particules de sol brisé se contractait tout en produisant un cisaillement le long de l'interface pile-sol. Ce mécanisme offre une explication de la dégradation de la friction du tronc à un horizon de sol donné avec pénétration accrue de la pile ('fatigue de pile') et une récupération consécutive de la capacité dans le temps ('reprise').

INTRODUCTION

The axial capacity of displacement piles in sand is arguably the subject of greatest uncertainty in geotechnical engineering (Randolph *et al.*, 1994). The most widely used technique for the design of long offshore displacement piles is that proposed by the American Petroleum Institute (API, 1993). However, a large variation in $Q_{predicted}/Q_{measured}$ is exhibited by this method when compared with a comprehensive database of load tests (Chow, 1997).

A number of approaches exist for predicting the base resistance of piles in sand. Analyses that use slip planes and bearing capacity theory to link friction angle with base resistance (e.g. Berezantzev *et al.*, 1961) do not capture the trends observed in the field. Alternative methods range from wholly empirical methods (e.g. API, 2000), based on soil type and relative density, to theoretical analyses based on cavity expansion (e.g. Randolph *et al.*, 1994) or strain path methods (Baligh, 1985). However, these methods also exhibit significant unreliability, and make contradictory assumptions regarding the failure mechanism, indicating that the correct link between soil properties and base resistance has not yet been identified. A recent prediction contest confirmed that pile design methods remain highly unreliable (Jardine *et al.*, 2001).

Improved reliability can be achieved by using cone penetration test (CPT) data instead of soil properties for design. This approach bypasses the need to assume a penetration mechanism. For example, by linking base resistance, q_b, to CPT resistance, q_c, the MTD Method (Jardine & Chow, 1996) can be used to predict base resistance in silica sand with a higher reliability than the API method (coefficient of variance (COV) in $Q_{predicted}/Q_{measured} = 0{\cdot}20$ when measured against the database assembled by Chow, 1997). This improved reliability is achieved by introducing a scale effect in which q_c is factored down by the ratio $[1 - 0{\cdot}5 \log(D/D_{cpt})]$. The mechanistic origin of this scale effect is unclear, and indeed an opposite scale effect has been observed in small-scale centrifuge modelling (Klotz & Coop, 2001). A number of alternative reduction factors to convert q_c to q_b, based on different mechanistic hypotheses, have been suggested (Winterkorn & Fang, 1975; Tejchman & Gwizdala, 1979; Kraft, 1990; Lee & Salgado, 1999; Borghi *et al.*, 2001; White & Bolton, 2004).

The observed unreliability in pile design methods suggests that the governing behaviour is not well understood. There is no consensus for the mechanism by which a pile penetrates sand or for the soil properties that govern this behaviour.

This paper describes a series of plane-strain calibration chamber tests in which the penetration mechanism of a displacement pile is observed, allowing displacement and strain paths to be measured. Previous attempts to quantify these soil movements (e.g. Robinsky & Morrison, 1964; Mikasa & Takada, 1973; Davidson *et al.*, 1981; Allersma, 1988; Chong, 1988) have been hampered by poor measurement resolution, the need to use artificial 'soil' material, and

Manuscript received 17 February 2003; revised manuscript accepted 14 April 2004.
Discussion on this paper closes on 1 March 2005, for further details see p. ii.
* Department of Engineering, University of Cambridge, UK.

the inability of the apparatus to replicate field stress levels around the pile tip. These disadvantages are overcome through the development of an image-based deformation measurement system based on particle image velocimetry and close-range photogrammetry (White *et al.*, 2003), and the construction of a reinforced plane-strain calibration chamber capable of revealing the soil surrounding the tip of a displacement pile while resisting the high penetration-induced stresses. It is noted, however, that plane-strain geometry causes ground movements to extend further from the pile than would occur in axisymmetry. For the case of an infinitely long pile installed in incompressible soil, lateral movements are inversely proportional to distance from the pile, whereas in plane-strain they are constant.

CALIBRATION CHAMBER

Calibration chambers are widely used to study penetration resistance (e.g. Houlsby & Hitchman, 1988; Yasufuku & Hyde, 1995; Salgado *et al.*, 1997). The stresses and deformations around the tip of an advancing CPT or pile can be correctly replicated by applying a surcharge pressure at the boundary of the chamber. In this research, a plane strain chamber with observation windows has been constructed in order to observe the soil deformation around an advancing pile (Fig. 1). The front face of the box includes six viewing windows through a 72·8 mm thick Perspex sheet. These viewing windows allow observation of the advancing pile and the resulting soil movement. The Perspex sheet is supported by a grillage of deep I-section steel straps to minimise out-of-plane deflections. Sheets of 4 mm thick glass are placed on the inner faces of the box to reduce side friction. As the sand–glass interface friction angle is significantly lower than the soil friction angle, failure will occur at the interface rather than within the soil body. This, coupled with the tight fit of the model pile between the front and rear faces of the chamber, ensures that the ground movement observed at the window is equal to that present through the soil model.

The internal width of the box is 1000 mm. Two breadths of model pile were tested: 32·2 mm and 16·1 mm, corresponding to ratios of chamber width to pile breadth of 31 and 62 respectively. The model pile was jacked into the chamber by a machine screw actuator driven by a stepper motor through a reduction gearbox.

The model piles were machined from Duraluminium, and fitted with 3 mm thick stainless steel base plates. A button load cell was mounted within the base plate with the active face machined flush with the base. A narrow hole was drilled longitudinally through the pile to carry the load cell wiring. After assembly of the chamber, the rear face of the pile was machined to provide a tight fit across the width. The pile surface was machined in the vertical direction. The resulting roughness was measured using a scanning white light interferometer. The mean roughness, R_A, measured at 10 locations on the pile surface was found to be 0·326 μm parallel to machining, that is, in the vertical direction during installation, and 1·424 μm perpendicular to machining. These values compare closely with other reported model pile tests, which typically use piles of roughness 1–2 μm (Bruno, 1999; Klotz, 2000). The tip of the pile was fitted with a driving shoe for test T7-DBS-45-shoe. The driving shoe consisted of the standard base plate, extended to overhang either side of the pile by 4 mm.

TEST SANDS

The mechanical behaviour of sands is usually considered to depend on whether or not the particles are crushable, with existing literature making a sharp distinction between the two. This has derived from the historic tendency for sands to be tested at stresses that are too low for the clearly defined common reference states of a linear critical state line (CSL) and a normal compression line (NCL) to be reached (e.g. Airey *et al.*, 1988).

Instead, in very general terms, crushable sands have been characterised by high peak angles of friction, which decrease with stress level and decay sharply with shear strain (Yasufuku & Hyde, 1995). Compression of crushable sands leads to significant volume change due to particle breakage, which offsets the influence of dilation due to rearrangement. Uncrushable sands are characterised by a smaller variation in angle of friction with stress level and very high volumetric stiffness. Significant dilation occurs during shearing of dense samples.

However, when taken to high stresses such as those induced by pile installation, sands that are considered crushable, as well as those not normally thought so, reveal similar patterns of behaviour. These patterns have much in common with critical state soil mechanics, and are often related to particle breakage (Coop, 1990). Two sands were selected for this research project, representing two extremes of mineralogy and particle strength: Dog's Bay carbonate sand (DBS) and Leighton Buzzard Fraction B silica sand (LBS).

Dog's Bay sand is of biogenic origin with 88–94% carbonate content (Houlsby *et al.*, 1988), and consists of broken shell fragments. The mechanical properties have been reported by Golightly & Hyde (1988), Coop (1990), Yasufuku & Hyde (1995) and Jovičič & Coop (1997).

It should be noted that previous research has been conducted using different gradings of Dog's Bay sand. The research described in this dissertation was carried out using a natural grading of Dog's Bay sand after passing through a 1·18 mm sieve to remove the gravel fraction. Index properties are shown in Table 1, and a photograph of typical grains is shown in Fig. 2(a).

Leighton Buzzard sand (LBS) has been widely used in research for the past 50 years, and is a rounded silica sand (Fig. 2(b)). Although no longer quarried from Leighton Buzzard, the material originates from the same geological deposit, the Lower Greensand. Fraction B is the 0·6–1·18 mm sieve fraction, and is often referred to as 14/25. The mechanical behaviour of this fraction has been investigated by Stroud (1971), Budhu (1979), Lee (1989) and Schnaid (1990). Index properties of the sand used in this research are shown in Table 1. For both sands, the maximum voids ratio was found using the procedure described in BS 1377 (BSI, 1990). To avoid grain crushing, the minimum voids ratio was found by vibrating a 1 kg sample without the use of a surcharge weight. The resulting values match closely with those previously published (e.g. Stroud, 1971; Golightly & Hyde, 1988).

TEST PROCEDURE

A series of eight tests is reported, each using dry sand (Table 2). The tests are identified by a code comprising the test number, sand type (DBS: Dog's Bay sand, LBS: Leighton Buzzard sand) and relative density. The suffixes 'shoe' and 'narrow' denote the tests with a pile shoe and half-width pile respectively. In each case, the model pile was jacked monotonically from the surface of the sample. During the first six tests, the initial state of the sand was varied and both silica and carbonate sands were used. Two additional tests were conducted: one test using the narrower pile (16·1 mm breadth), and one test in which the broad pile was fitted with a driving shoe.

The sand sample was prepared by pluviation in air, with drop height and flow rate varied to achieve the desired initial

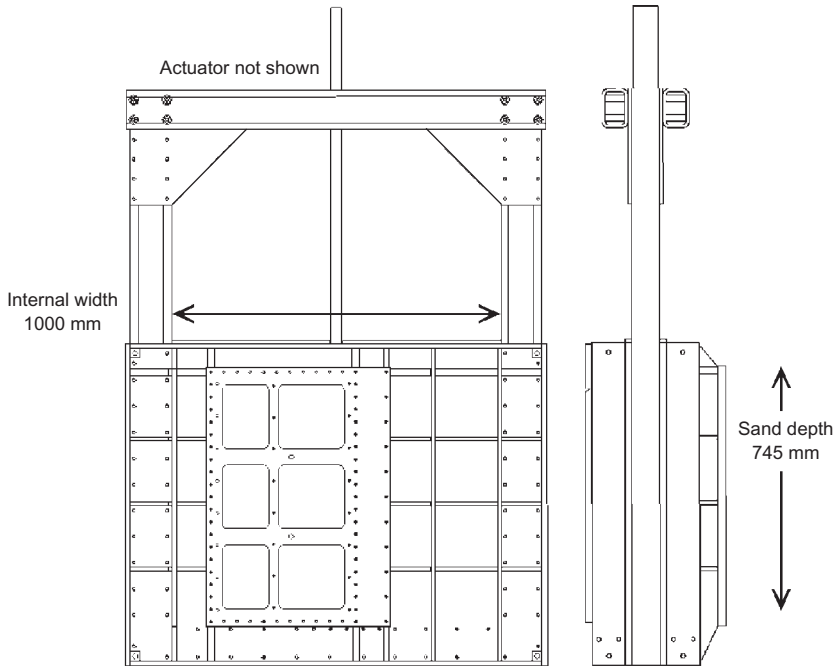

(a)

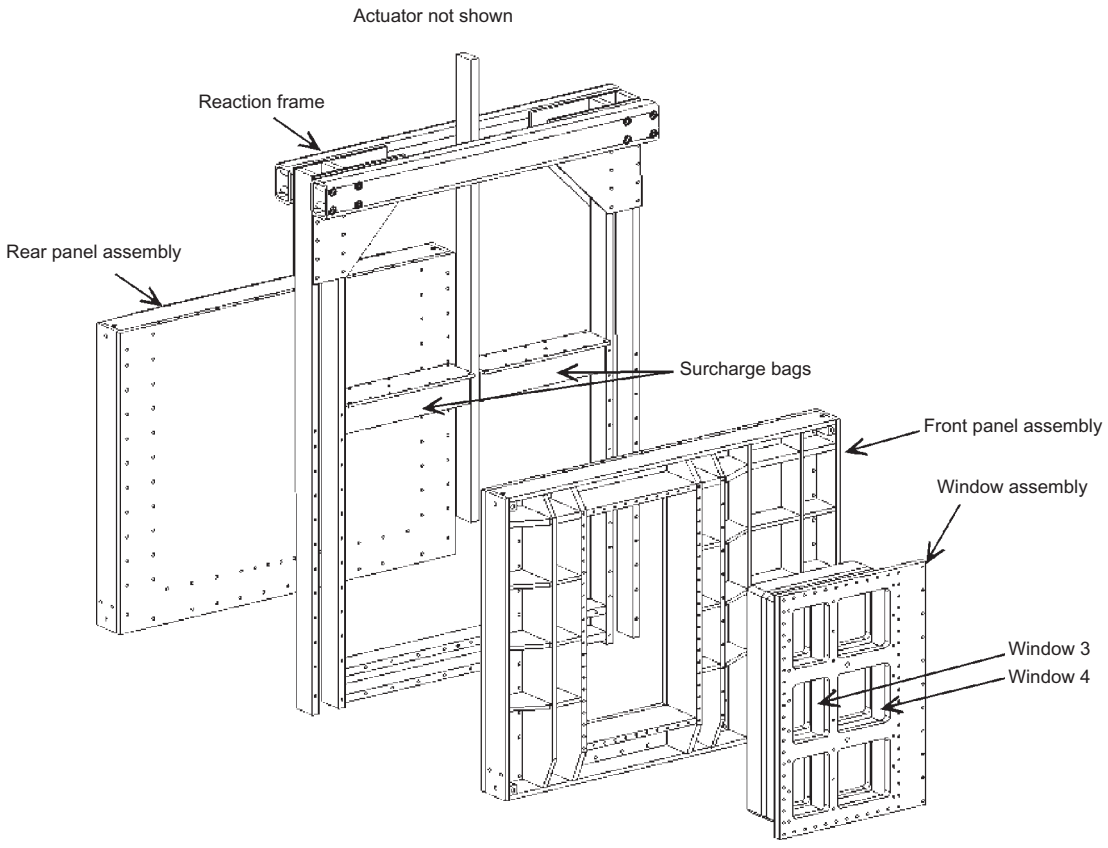

(b)

Fig. 1. Schematic arrangement of calibration chamber: (a) front and side projections of assembled chamber; (b) exploded view of chamber components

Table 1. Index properties of test sands

Sand	Mineralogy	G_s	D_{50}: mm	e_{max}	e_{min}
Dog's Bay sand	Calcium carbonate	2·75*	0·44	1·87	0·98
Leighton Buzzard Fraction B	Silica	2·65†	0·84	0·80	0·51

*From Golightly (1989).
†From Tan (1990).

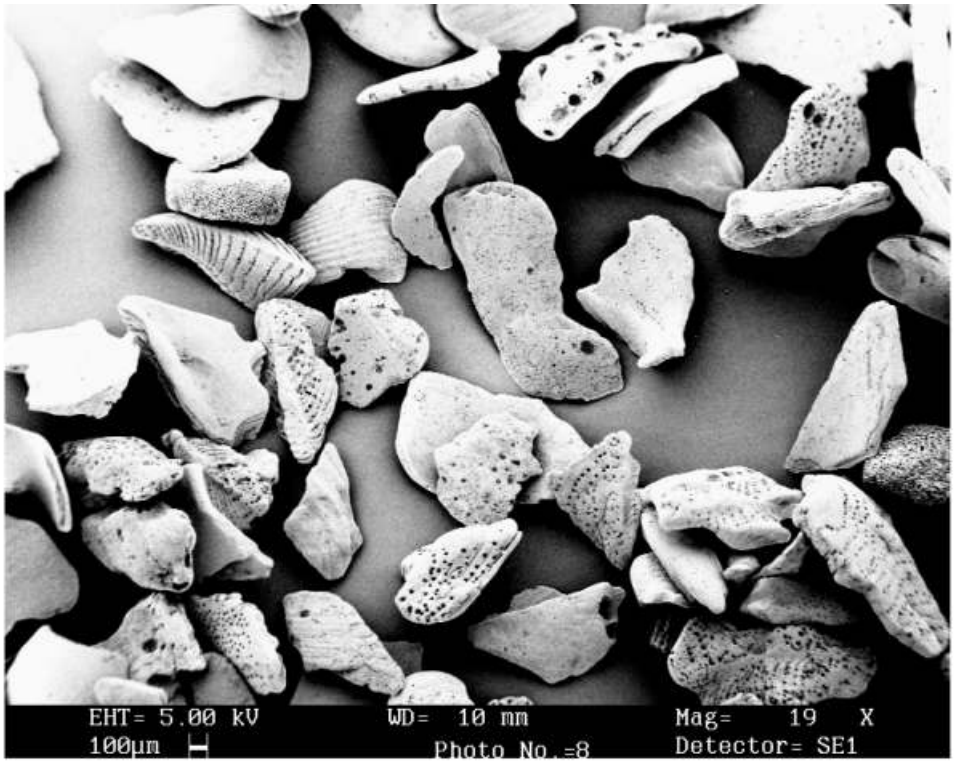

(a)

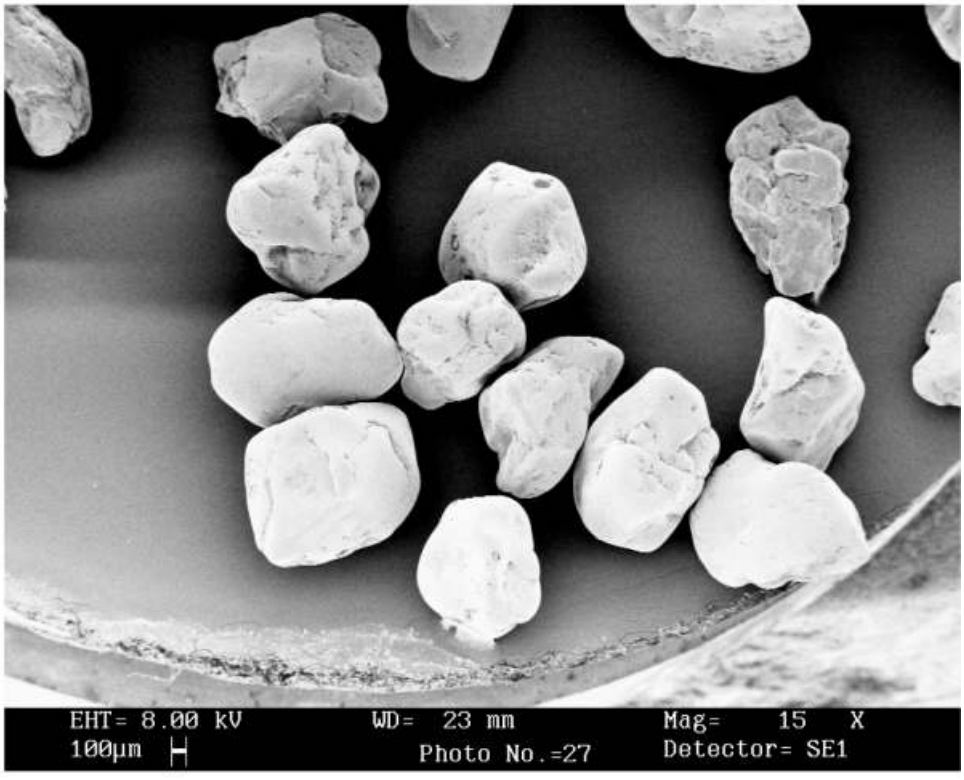

(b)

Fig. 2. SEM image of each test sand: (a) Dog's Bay carbonate sand (SEM image from Bowman *et al.*, 2001); (b) Leighton Buzzard Fraction B silica sand (SEM image from Sentenac *et al.*, 2001)

state. Each model was poured in lifts of approximately 50 mm with density checks carried out after each lift. The relative density of lifts within a single model fell within a range of ±2%. A surcharge of 100 kPa was applied to the top surface of the sand, and reduced to 50 kPa.

The model pile was jacked into the chamber at a rate of 1 mm/min. Digital cameras were used to record images of the soil and pile at regular intervals. A button-type load cell installed in the tip of the model pile recorded base resistance, q_b, throughout installation. Feedback from the stepper

Table 2. Calibration chamber test series

Test code	Sand type	Initial voids ratio, e_0	Relative density: %	Pile breadth: mm	Pile tip configuration
T1-DBS-64	DBS	1·30	64	32·2	Flat ended
T2-DBS-44	DBS	1·48	44	32·2	Flat ended
T3-DBS-71	DBS	1·24	71	32·2	Flat ended
T4-LBS-34	LBS	0·70	34	32·2	Flat ended
T5-LBS-55	LBS	0·64	55	32·2	Flat ended
T6-DBS-84	DBS	1·12	84	32·2	Flat ended
T7-DBS-45-shoe	DBS	1·47	45	32·2	Driving shoe
T8-DBS-46-narrow	DBS	1·46	46	16·1	Flat ended

motor was used to monitor the pile tip depth, with cross-checks made from the camera images.

A set of image control points was installed within each porthole in the viewing window. These control points were laser-printed onto overhead transparency sheets and measured using a calibrated photogrammetric target to establish their exact locations, eliminating errors due to inaccurate laser printing. These control points were used to establish the photogrammetric transformation parameters required to convert image-space PIV measurements of soil movement into object-space coordinates (White *et al.*, 2003). The overhead transparency sheets were installed between the Perspex window and the glass sheets. An appropriate refractive correction was included in the transformation to account for the offset distance between the observed plane of soil and the plane of the control points.

TEST RESULTS

The primary source of data in each test was the images captured through the viewing portholes. Soil displacement and strain paths around the advancing pile were measured from these images. In addition, the load cell in the pile base indicated the q_b–depth profile. Fig. 3 shows the variation of q_b with pile tip depth for each test. Within each test there is a general trend of sharply increasing base resistance during the first 30–50 mm of penetration, during which the pile can be considered as a shallow foundation, followed by a more steady response. An approximately constant value of q_b and therefore a steady-state penetration mechanism was reached during the tests on DBS.

During the LBS tests, a constant value of q_b was not reached. During the loose test (T4-LBS-34) an increase in q_b of 32% was recorded between depths of 100 mm and 440 mm. The rising gradient of the q_b–depth curves for the LBS tests indicates that a steady state is not being approached. This trend could derive from an increasing influence of the chamber base with pile tip depth, as the influence of a remote rigid boundary would be larger in the stiff silica sand than in the compressible carbonate sand. Klotz & Coop (2001) also observed boundary effects when installing model piles in LBS, whereas tests in DBS using the same chamber appeared unaffected. Test T5-LBS-55 was halted at a depth of 301 mm, as the base resistance was approaching the maximum design load of the chamber.

The steady-state values of base resistance reached during the DBS tests allow the influence of initial soil state to be examined. A trend of increasing q_b with initial relative density is evident from Fig. 4. If it is assumed that the ambient vertical stress in the region of steady-state penetration is 50 kPa, the bearing capacity factor, N_q, varies in the range 36–116 between relative densities of 44% (T8-DBS-46-narrow, q_b = 1·82 MPa) and 84% (T6-DBS-84, q_b = 5·8 MPa). As would be expected, significantly higher base resistance is measured in LBS than in DBS. At a pile tip depth of 100 mm the base resistance in tests of comparable relative density differs by a factor of 6–8.

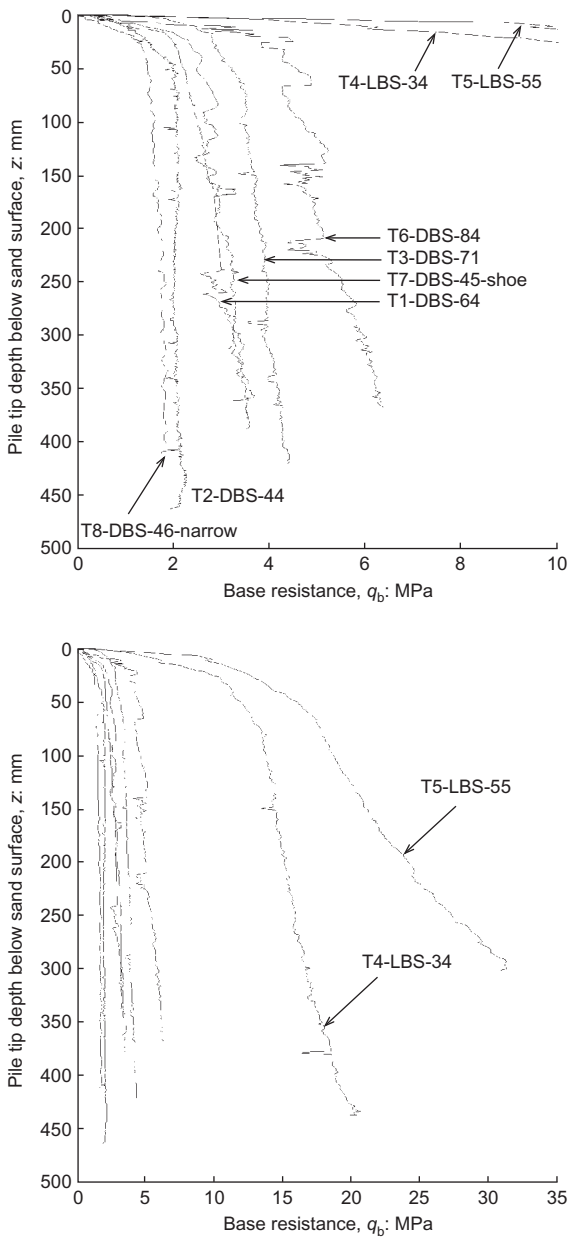

Fig. 3. Base resistance, q_b, plotted against pile tip depth during installation

PHOTOGRAPHIC DATA

The technique used to measure soil displacement from digital images is described by White *et al.* (2003). This

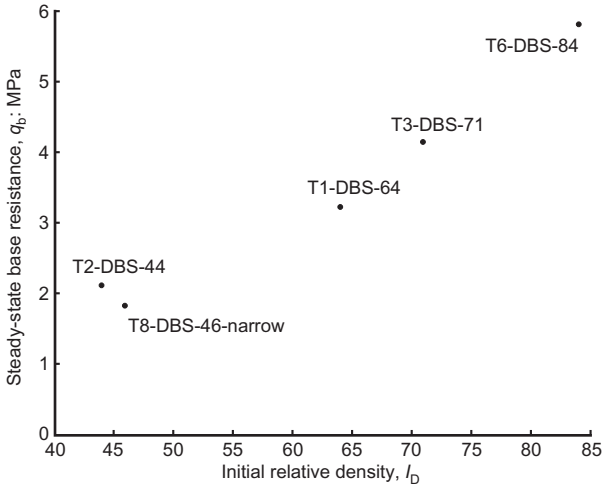

Fig. 4. Variation of steady-state base resistance with relative density

technique combines particle image velocimetry (PIV) and close range photogrammetry to achieve significantly higher accuracy and precision than previous methods used in geotechnical modelling, without requiring target markers to be installed in the observed soil.

The following measurements were deduced from the captured images (White, 2002):

(*a*) soil displacement during pile installation
(*b*) soil strain paths during pile installation
(*c*) streamlines of soil flow
(*d*) soil strain post-installation (i.e. as would be the case prior to loading of pile)
(*e*) soil movement adjacent to pile shaft.

Limitations of space prevent this paper from containing all the above measurements from each test. Selected measurements are presented in order to establish:

(*a*) the influence of the chamber boundaries
(*b*) the mechanism of penetration, by which base resistance is created
(*c*) the soil movement adjacent to the pile shaft, which strongly influences shaft friction.

Images were captured at pile tip displacement increments of 1–2 mm. A typical image, from test T2-DBS-44 captured at a pile embedment of 300 mm, is shown in Fig. 5, overlain by a mesh of 20 × 20 pixel PIV test patches. Each PIV patch is nominally 2·5 mm × 2·5 mm in size, covering only a few individual grains. As a result, the 'gauge length' between adjacent displacement measurements, from which strains are calculated, is too small for a smooth strain path to be expected. In the same manner, a smooth stress–strain curve would not be expected from an element test of dimensions 2·5 × 2·5 mm.

DISPLACEMENT PATHS DURING PILE INSTALLATION

The most straightforward illustration of the penetration mechanism is the displacement field around the pile tip. Fig. 6 shows the displacement field found from comparison of the PIV mesh shown in Fig. 5 with a subsequent image, captured after 1·5 mm of pile tip movement. This displacement field consists of 3901 vectors, which have been enlarged to reveal the deformation pattern. Fig. 7 shows the magnitude of the displacement vectors in Fig. 6, indicating the extent of the displacement field. Although the deformation consists primarily of downward movement below the pile, horizontal displacements of 25 μm are detected in the far field, at an offset of 160 mm (≈ 5*B*) from the pile centreline.

There is no evidence of a bearing capacity-type mechanism in which the soil flows along streamlines curving from

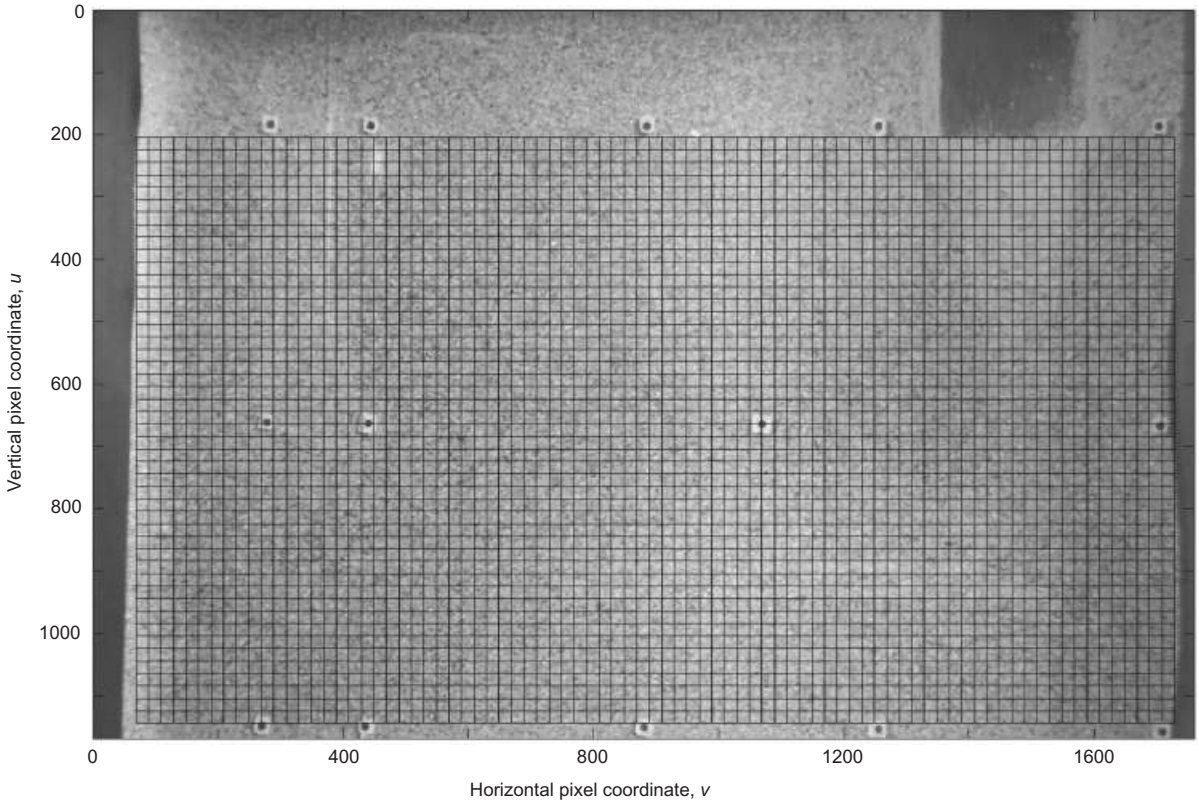

Fig. 5. Typical PIV mesh

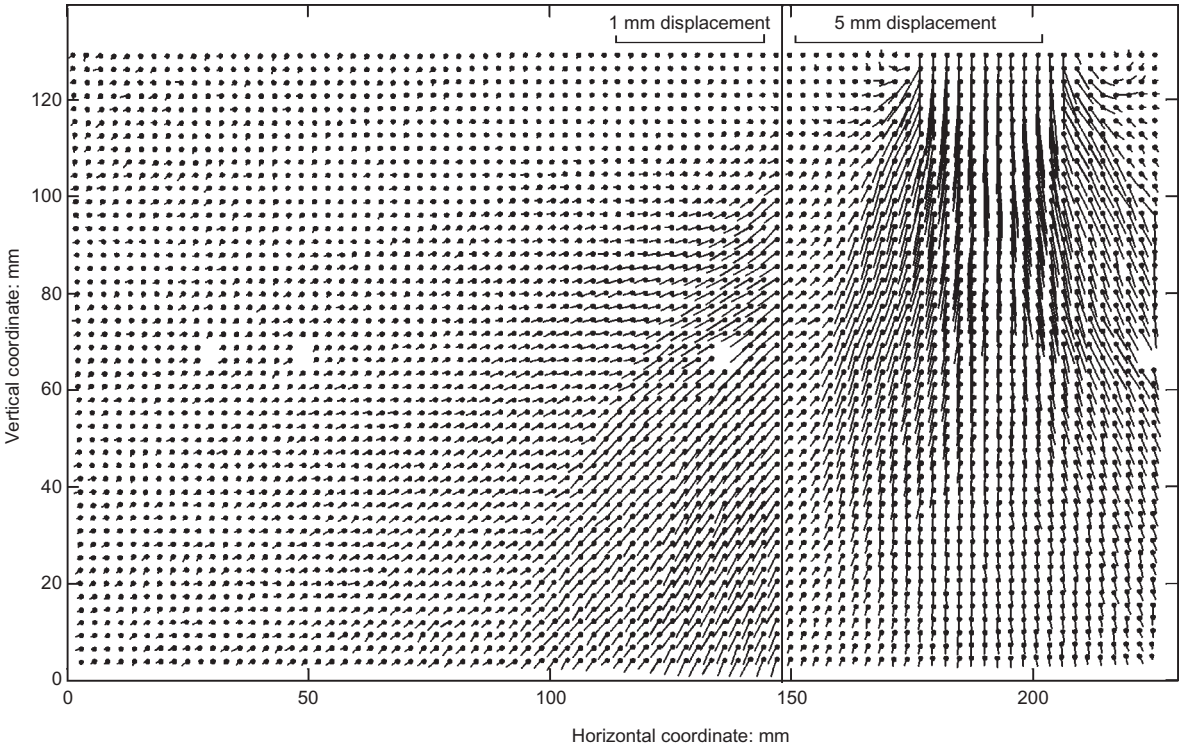

Fig. 6. Displacement field around pile tip

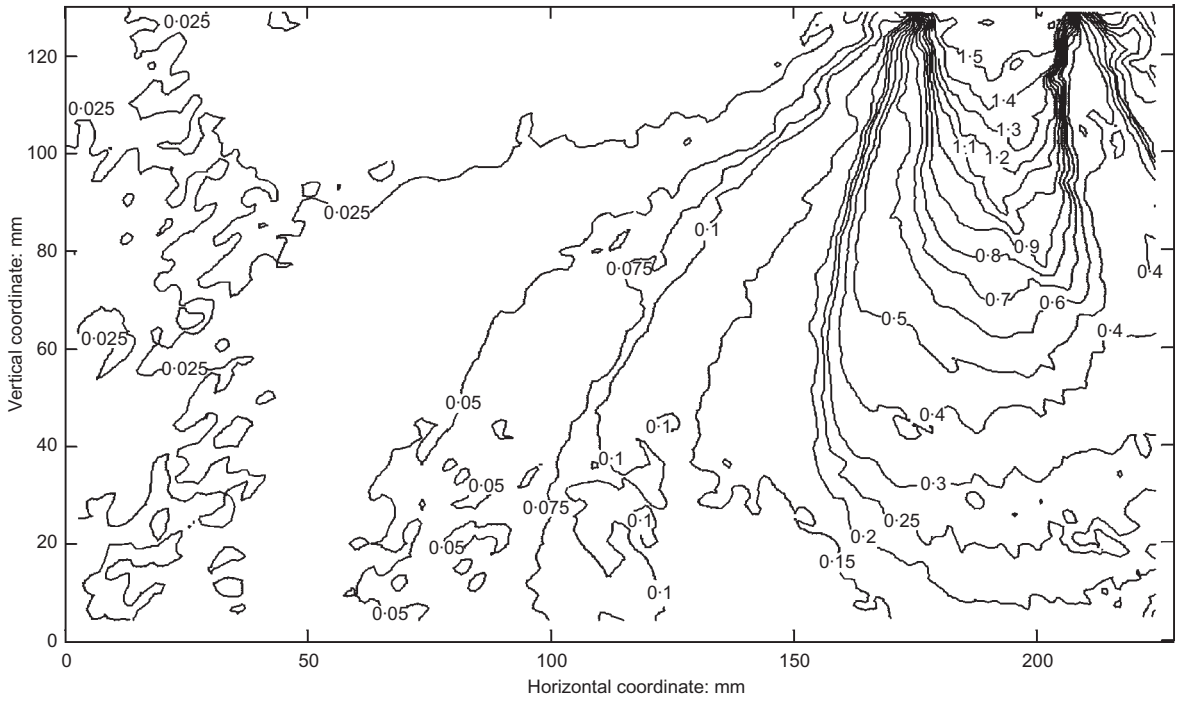

Fig. 7. Contours of displacement field magnitude

below the pile tip around to the upward direction on either side of the shaft. The penetration mechanism is more comparable to cavity expansion, with the displacement vectors radiating from the pile tip downwards and to the side. However, although the contours of displacement follow a circumferential path immediately below the pile, these contours return to the pile shoulder. This sharp variation in instantaneous velocity with inclination from the vertical is in contrast to a cavity expansion model for penetration, in which all components are assumed to vary only with the radial coordinate.

Figure 8 shows the full displacement trajectories of two soil elements tracked through tests T2-DBS-44 and T4-LBS-34. The coordinate origin is located on the centreline of the pile and level with the pile tip at the end of installation. As the pile approaches, the movement is generally downwards, with the soil element trajectory curving towards the horizontal as the pile passes. In the case of LBS, the final part of

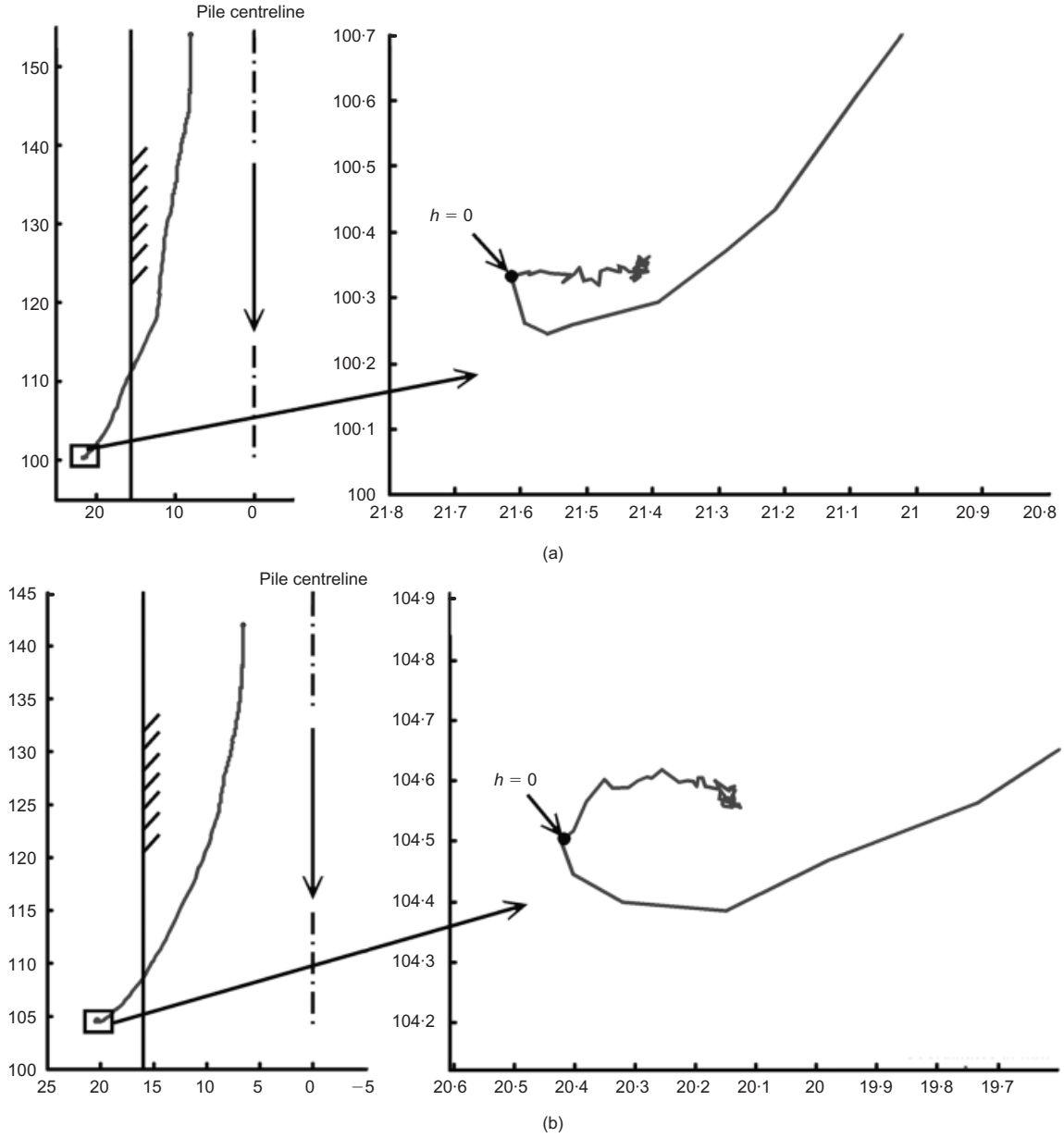

Fig. 8. Soil element trajectories during pile installation (coordinates in mm): (a) T2-DBS-44; (b) T4-LBS-34

the element trajectory is upwards, although the net movement is downwards, in contrast to bearing capacity mechanisms, which rely on soil heave to accommodate the pile volume. Greater net downward movement and less net lateral movement is observed in DBS than in LBS.

A notable feature of Fig. 8 is the 'tail' at the end of each trajectory. After the pile tip has passed the soil element (i.e. $h > 0$, where h is the vertical distance of a soil element above the pile tip), the soil relaxes back towards the pile shaft. This 'tail' in the displacement trajectory is examined more closely in connection with shaft friction later in this paper.

STEADY-STATE DEFORMATION

In Fig. 9 the displacement trajectories for the column of soil elements visible in window 4 and initially located at an offset of 1·15B from the pile centreline in tests T2-DBS-44 and T4-LBS-34 have been normalised by the half-breadth of

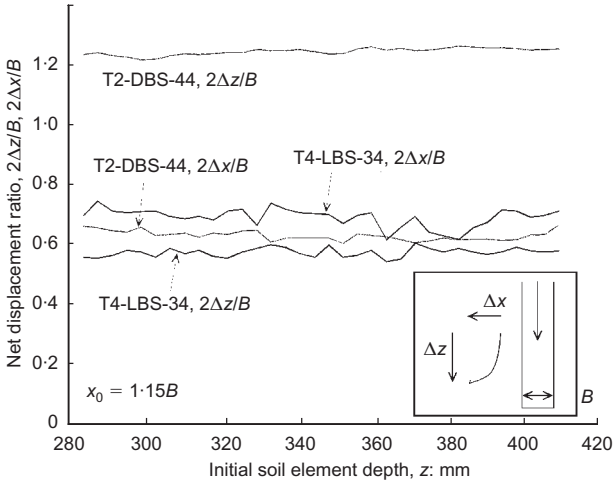

Fig. 9. Net displacement of a single column of soil elements

the model pile. The horizontal and vertical displacement ratios are defined as the net horizontal movement, Δx, and net downward movement, Δz, during installation of the pile (until $h = 0$), normalised by the pile half-breadth, $B/2$. Fig. 9 demonstrates the steadiness of the deformation pattern; there is no systematic trend for $2\Delta x/B$ or $2\Delta z/B$ to increase or decrease with depth as the pile passes the viewing window.

Figure 9 does reveal some random variation in displacement ratio of approximately $\pm 0{\cdot}03$, which is equal to a displacement of ± 400 μm—approximately one particle diameter. Random noise of this magnitude is to be expected, considering that the PIV patch size is equivalent to a few particle diameters. It is highly conceivable that while being displaced by 55 mm (>125 particle diameters) during installation of the pile, as shown in Fig. 8, adjacent groups of four to seven particles may become separated from their neighbours by a particle diameter. The assumption of continuum behaviour therefore breaks down, and adjacent pairs of soil elements cannot be used to generate continuum strain paths for the bulk material.

The steady-state deformation pattern shown in Fig. 9 shows that displacement trajectories for a given value of h will be the same, independent of the original depth of the soil element. Therefore all trajectories from a single column of soil elements can be combined to provide the deformation pattern over a greater vertical extent below the pile tip than is visible at any given instant.

The viewing window only allows a vertical extent of 160 mm ($5B$) to be simultaneously observed. However, by combining the displacement data during installation found from all soil elements originally located within a single vertical column, the penetration mechanism can be inferred over a greater vertical extent. Furthermore, this method of combining the data from multiple patches allows strain measurements representative of the continuum behaviour to be obtained.

This transformation is equivalent to describing every soil element trajectory using a reference frame with the origin located at the tip of the pile (on the centreline). The penetration mechanism is then viewed as the steady flow of soil around a stationary pile. The coordinate axes consist of the horizontal offset from the centreline, x, and the vertical distance above the tip of the pile, h (h is positive upwards).

To make clear the distinction between x–y plots of displacement data from individual patches (as shown in Figs 6–9), and x–h plots that have been assembled by combining the data from multiple patches in the column-wise manner described above, all x–h plots (Figs 16–19) are presented as mirror images with the pile on the left-hand side. In this mode of presentation the x-axis is positive in the left-to-right direction.

NET SOIL MOVEMENT DURING INSTALLATION

Figure 10 shows the variation in horizontal and vertical displacement ratio with initial offset from the pile centreline, $2x_0/B$, for tests T2-DBS-44 to T8-DBS-46-narrow, using data both from window 4, through which the pile can be observed, and from window 3, through which the far-field behaviour ($x_0 = 6{\cdot}5B$–$12B$) can be seen.

It is evident from Fig. 10 that the end wall of the chamber has an influence on the displacement field around the pile. All curves for horizontal displacement ratio tend towards zero at $2x_0/B \approx 31$, which corresponds to the end wall position. The exception is test T8-DBS-46-narrow. In this case, the end wall is located at $2x_0/B = 62$, towards which the horizontal displacement tends to zero. This observation demonstrates that plane-strain geometry requires a much more conservative ratio of chamber to pile size than axisymmetric geometry (e.g. Bolton *et al.*, 1999) if the displacement field around the pile is to be entirely uninfluenced by the chamber boundaries. The horizontal displacement ratio close to the pile shaft during test T8-DBS-46-narrow converges towards the data from tests conducted using the larger pile, suggesting that although the far-field behaviour is affected by the end wall, the influence in the near field is minimal.

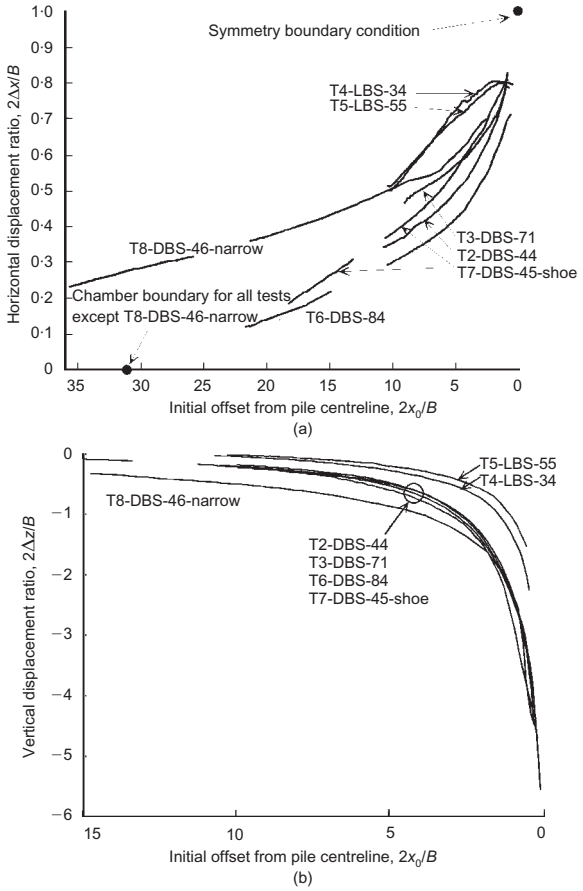

Fig. 10. (a) Horizontal and (b) vertical displacement during pile installation

The curves of displacement ratio shown in Fig. 10 divide by soil type. The zone of horizontal deformation is concentrated closer to the pile shaft in compressible DBS than in LBS, and DBS is pushed downwards almost twice as far as the LBS. For both soils the zone of downward displacement is concentrated closely around the pile shaft, whereas the horizontal displacement decays slowly with offset distance.

For each test a network of triangular strain elements was constructed from the mesh of soil elements tracked by PIV. The procedure described in Appendix 1 was used to decompose the deformation into strain (or stretch) and rotation. Fig. 11 shows a zone of very high rotation (>20°) close to the pile ($2x_0/B < 2$), justifying the use of a finite rotation strain calculation. The rigid body rotation measured in DBS is approximately twice that measured in LBS at a comparable initial offset.

SOIL STRAIN PATHS DURING PILE INSTALLATION

The calculation procedure described in Appendix 1 converts the measured displacement trajectories into the strain paths induced by pile installation. In order to present the evolution of strain within a soil element as it flows towards and beyond the pile tip, strain paths are presented as shown

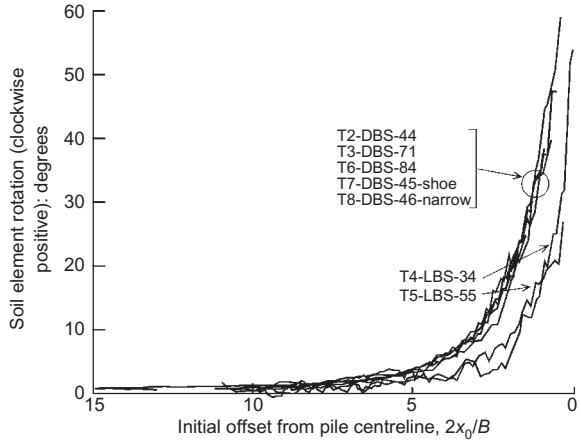

Fig. 11. Soil element rotation during pile installation

in Fig. 12, having been decomposed from rigid body rotation. Natural (or logarithmic) strains are used, as is conventional for large-strain behaviour, with compression positive. The position of the soil element is described by the h-coordinate, normalised by $B/2$. The strain quantities included on the plot are the cumulative horizontal and vertical strain, defined within the reference frame of the soil element. Also shown are the maximum and minimum principal strains. The evolution of these strain quantities can be regarded as the projection of a Mohr's circle of strain along the shear strain axis. This construction indicates the maximum shear strain by the width of the envelope created by ε_I and ε_{II}. It should be noted that, for very high values of natural strain, the usual construction of a Mohr's 'circle' does not apply. For example, the mean value of the principal strains is not equal to the mean value of the vertical and horizontal strains, as is the case for a small-strain formulation.

Figures 13 and 14 show strain paths for tests T2-DBS-44 and T4-LBS-34 from six different initial horizontal offsets from the pile centreline, corresponding to $2x_0/B \approx 1$, 2, 3, 4, 6 and 10. The variation of rigid body rotation with $2h/B$ for each initial offset is also shown. The volumetric strain paths are shown separately in Fig. 15. Volumetric strain is defined in the conventional manner as the change in volume expressed as a percentage of the original volume.

These six strain paths are divided into three zones of behaviour—'very near', 'near' and 'far' field—and discussed separately below. An additional zone of behaviour, referred to as the interface zone, lies immediately adjacent to the pile shaft. This zone extends horizontally by only 2–3 mm and therefore cannot contain sufficient PIV patches for strain paths to be calculated. Other evidence of the volume change behaviour within the interface zone based on post-test sampling is discussed later.

The very near field behaviour is indicated by the strain paths of soil elements originally located at $2x_0/B = 1$ and $2x_0/B = 2$. These strain paths reach values of natural direct strain greater than 50% in compression and 200% in extension, which far exceed the range of conventional laboratory element testing. The shape of the strain path in the near field is similar for both soil types. Below the pile tip the principal strain directions are approximately vertical and horizontal, as required for symmetry.

A reversal of the vertical strain rate from compression to extension occurs at $2h/B \approx -3$, followed by a reversal in the horizontal strain rate from extension to compression at $2h/B \approx -1$, accompanied by significant rotation. On passing the pile tip, the soil elements lie in horizontal extension relative to their initial state, albeit having rotated by as much as 45°. Although the general shapes of the strain paths in DBS and LBS are alike, the strain levels in the very near field are 30–50% higher in DBS for a given value of $2h/B$.

The near-field behaviour is indicated by the strain paths of soil elements originally located at $2x_0/B = 3$, 4 and 6. Once again, similar trends are observed in DBS and LBS. Within this range of offset the absolute values of strain are of comparable magnitude in both sands. Compared with the very near field, the change in direction of strain rate occurs earlier, and at the same point in both the horizontal and vertical directions. This is followed by strain sufficient to exceed the initial cycle. Both the horizontal and vertical strain paths return to and cross the strain axis. The final state is one of horizontal compression and vertical extension.

Shear strain continues to accumulate after reversal of the horizontal and vertical strain direction. The point at which horizontal and vertical strain are equal (and close to zero) corresponds closely with the point of maximum shear strain (i.e. maximum principal strain difference), indicating a state of almost pure shear.

The far-field behaviour is indicated by the strain paths of soil elements originally located at $2x_0/B \approx 10$. At this large offset from the pile shaft, the shape of the strain path differs slightly between DBS and LBS. In DBS the trend of initial horizontal extension followed by compression seen in the near field is again observed. In LBS the horizontal strain increases monotonically in compression. Also, the absolute

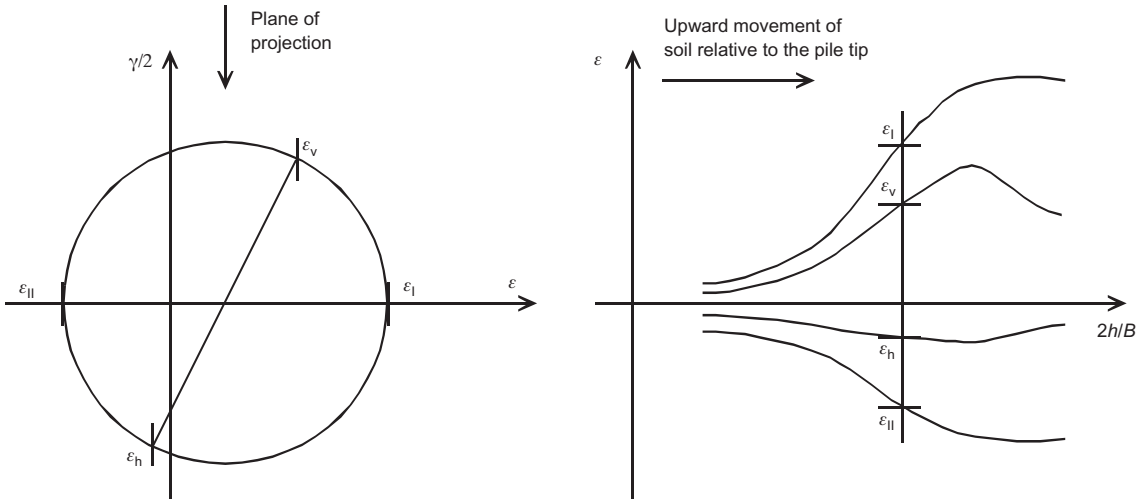

Fig. 12. Illustration of strain path by evolving Mohr's circle of strain

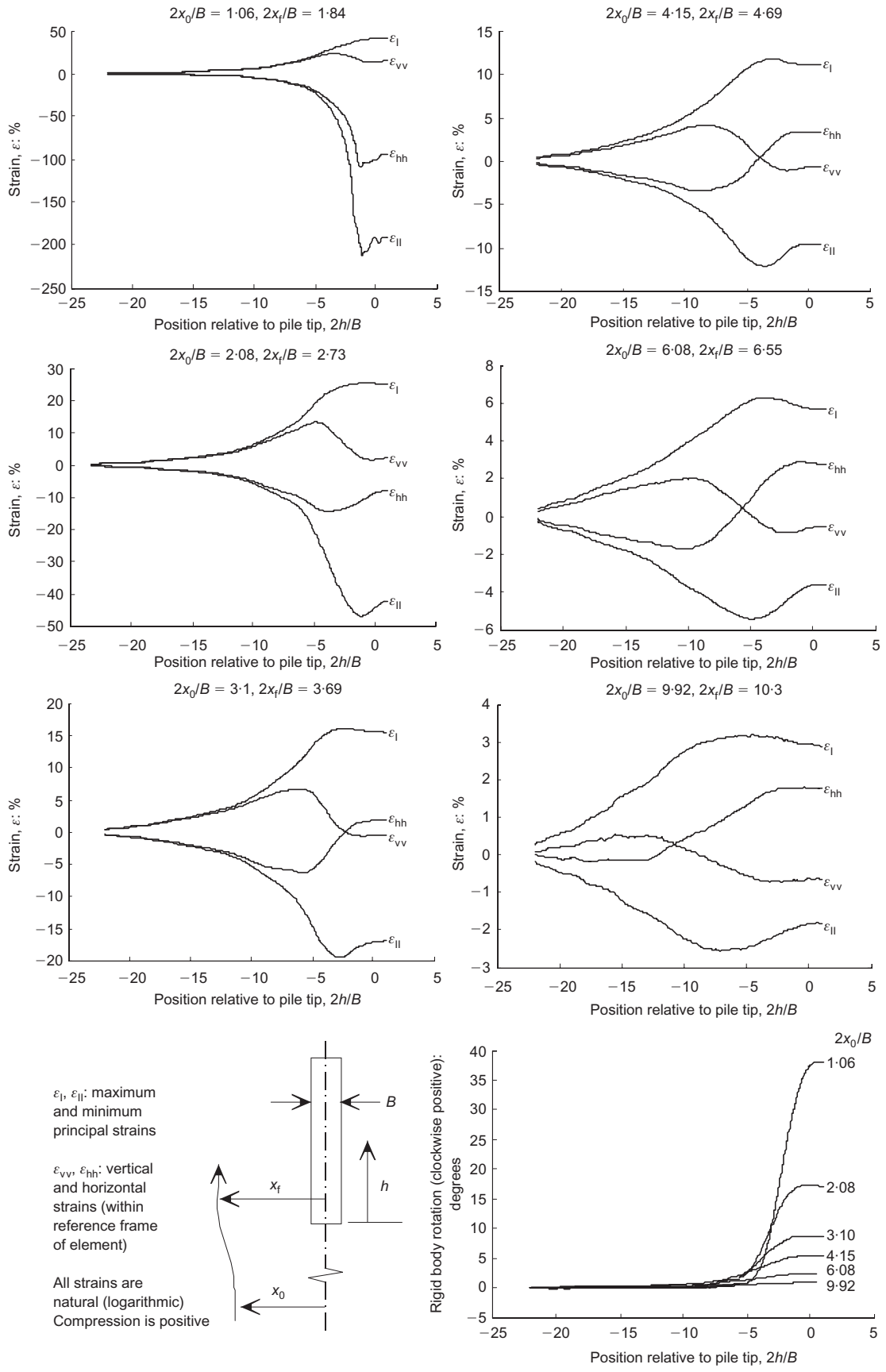

Fig. 13. Strain and rotation paths during pile installation: T2-DBS-44

strain levels in DBS are typically 50% lower than in LBS. This is in agreement with Fig. 10, in which the deformation is localised closer to the pile tip in DBS than LBS.

The volumetric strain paths in DBS and LBS show monotonically increasing compression with increasing $2h/B$ in both sands, with greater compression observed for DBS (Fig. 15). Immediately below the pile tip ($-4 < 2h/B < -1$), dilation is evident in the very near field ($2x_0/B < 2$),

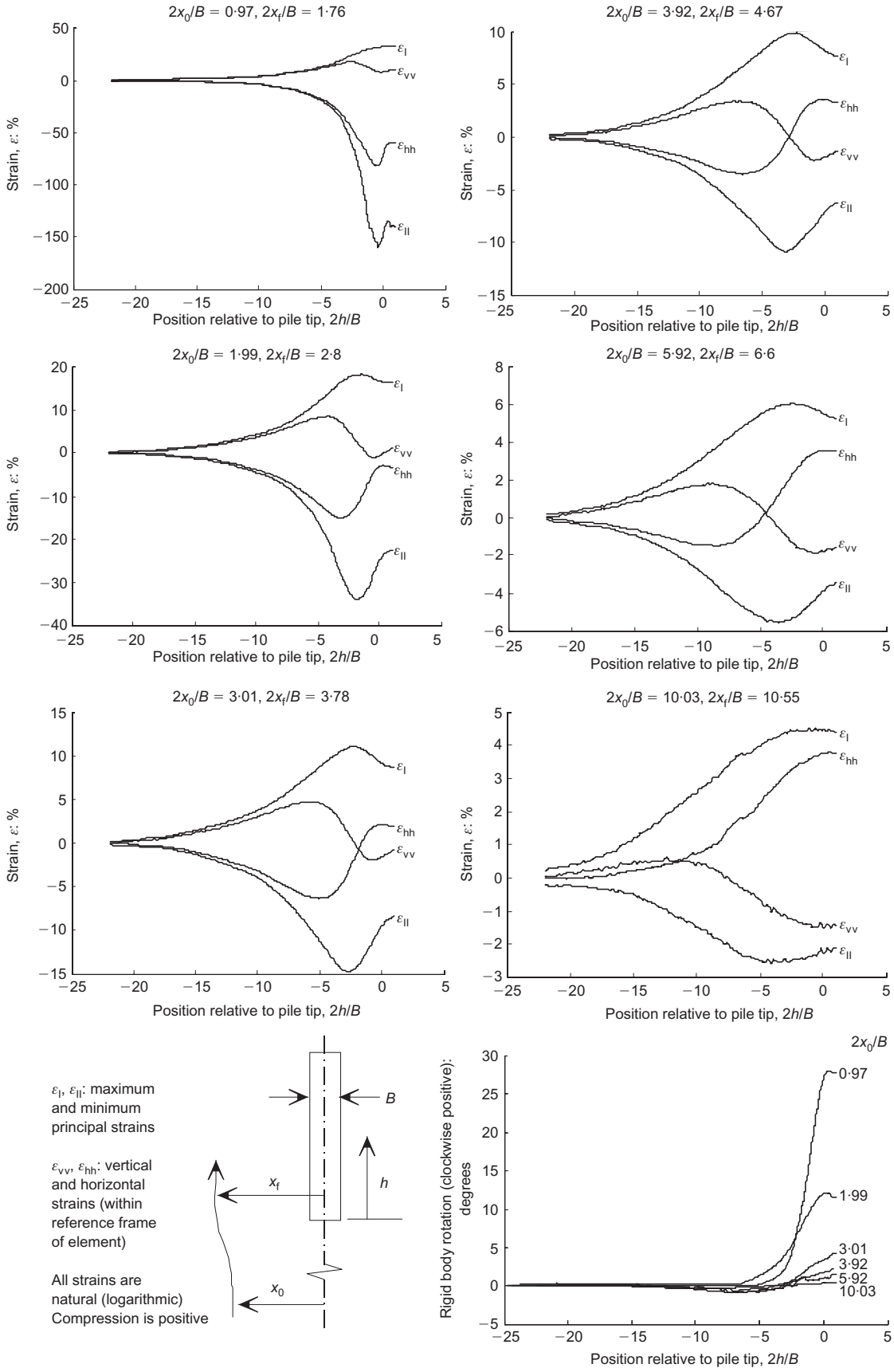

Fig. 14. Strain and rotation paths during pile installation: T4-LBS-34

followed by recompression as the soil element moves around the pile shoulder ($-1 < 2h/B < 1$). In DBS the soil remains in net compression for $h > 0$ despite this dilation cycle, whereas in LBS a net dilation of 1% is recorded for $2x_0/B = 0{\cdot}97$. The end points of the volumetric strain paths indicate the horizontal variation in density adjacent to the pile shaft (excluding the interface layer, which is discussed later). In DBS, despite the dilation around the pile shoulder,

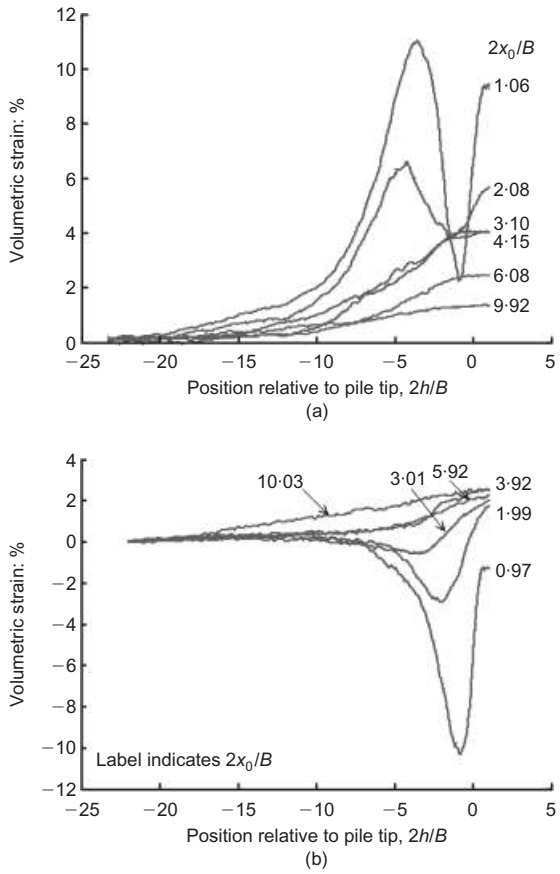

Fig. 15. Volumetric strain paths: (a) T2-DBS-44; (b) T4-LBS-34

there is a continual decrease in density with increasing offset. In LBS, the strong dilation in the near field creates a zone of soil close to the shaft that is less dense than the more distant soil.

STREAMLINES OF SOIL FLOW

The two strain reversal points corresponding to the maximum of ε_v and minimum of ε_h shown in Figs 13 and 14 are superimposed on the streamlines of soil flow in Fig. 16 for the full range of initial horizontal offset. These points are approximately coincident on each streamline, revealing two distinct zones of deformation. Below the pile and within a region bounded by a line inclined downwards at approximately 55° from the horizontal is a zone of soil that is undergoing vertical compression and horizontal extension. Above this region the strain rates are reversed. Close to the pile the strain reversal points do not coincide, and a short phase of both vertical and horizontal extension is observed. This corresponds to the zone of dilation evident in the volumetric strain paths.

POST-INSTALLATION STRAIN DISTRIBUTION

The strain paths presented in Figs 13 and 14 can be assembled as the strain distribution within the soil surrounding the pile after installation. This spatial distribution of strain also represents the initial conditions prior to application of a working load to the pile if the strain associated with removal of the installation force and during any interim creep period is ignored. The pile tip rebound during unloading of a field pile might typically be equal to 1 or 2 mm. This would induce strains in the surrounding soil approxi-

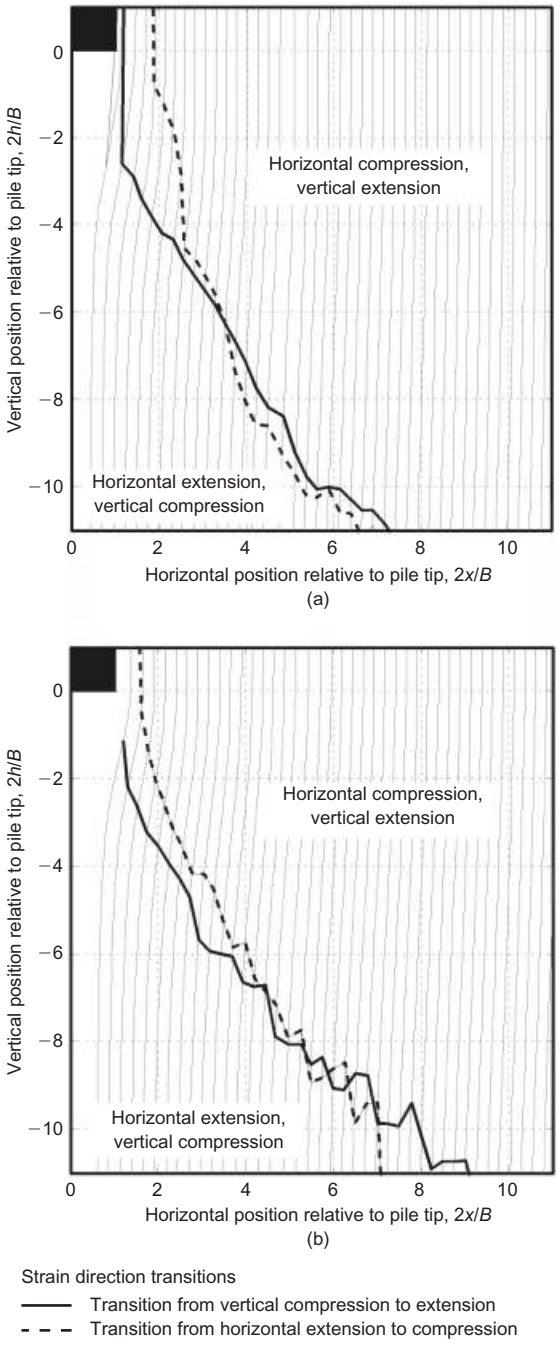

Fig. 16. Streamlines of soil flow and strain rate reversal points: (a) T2-DBS-44; (b) T4-LBS-34

mately equal to a short reverse excursion along the strain paths in Figs 13 and 14 by a distance equal to $2\Delta h/B = 0{\cdot}1$.

The spatial distribution of installation-induced strains has a strong influence on the settlement response of a displacement pile under working load. The base stiffness of a pile arises from integration of the stiffness contributions provided by the deforming soil around the pile: if this soil is to be modelled, appropriate stiffness values must be selected. A bored pile can be 'wished in place' and analysed, based on the assumption that installation-induced strains are small and negligible. In contrast, the strain paths shown previously indicate that the condition of the soil surrounding a displacement pile is significantly changed by the installation procedure. Soil stiffness is influenced by strain level (e.g. Jardine *et al.*, 1984) and recent loading direction (Atkinson *et al.*, 1990). These influences can be quantified from the strain distribution and the streamlines of flow.

Figures 17 and 18 show the spatial distribution of strain surrounding the base of the pile in tests T2-DBS-44 and T4-LBS-34. These are the tests for which strain paths were previously presented. In addition, the strain distribution from test T8-DBS-46-narrow is shown, to allow the influence of the ratio of chamber to pile size to be examined (Fig. 19). To provide clarity in areas of high strain gradient, the contour interval is varied from 0·5% in the far field to 25%

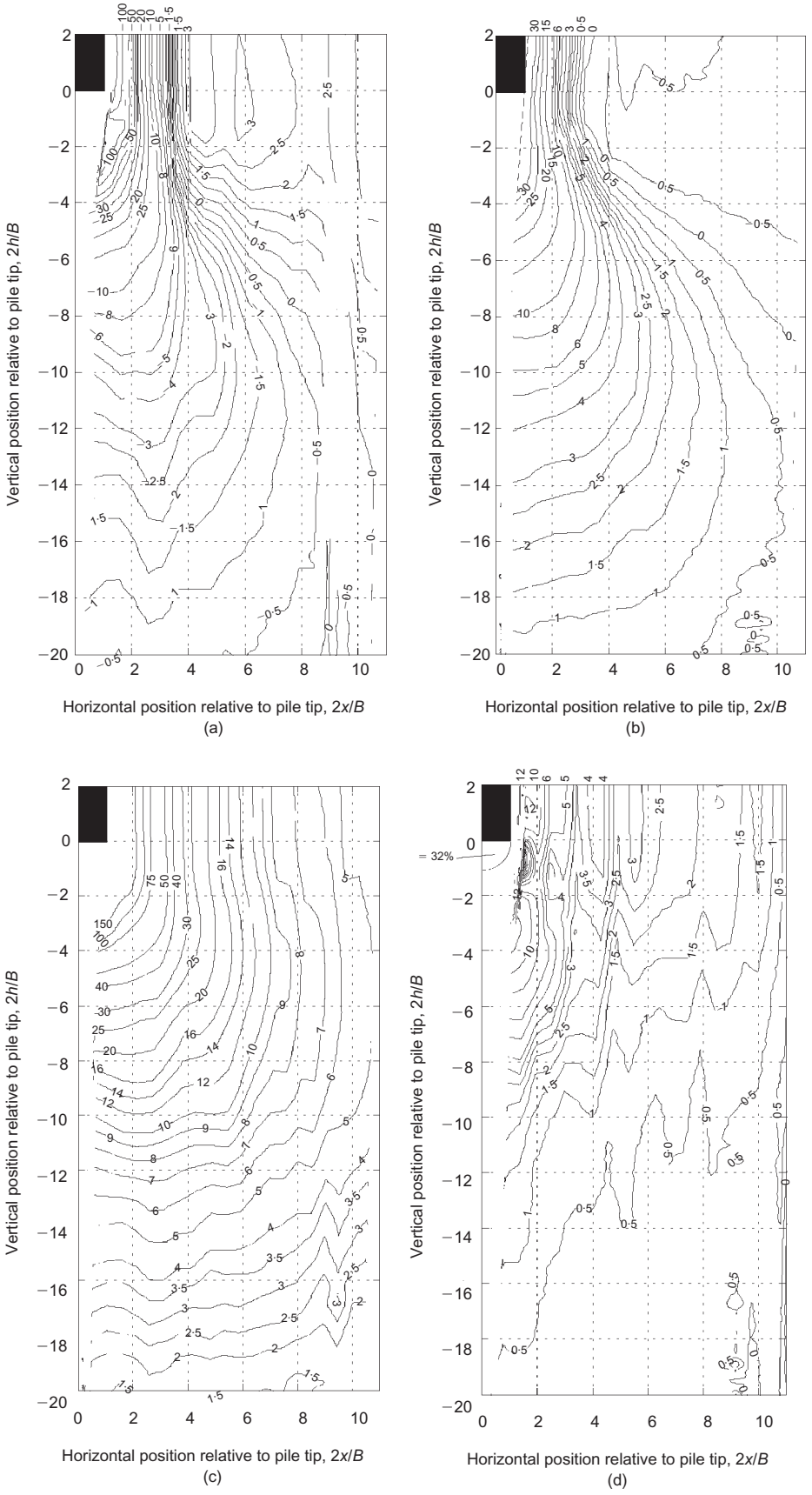

Fig. 17. Post-installation strain distribution, T2-DBS-44: (a) horizontal strain (%); (b) vertical strain (%); (c) maximum shear strain (%); (d) volumetric strain (%)

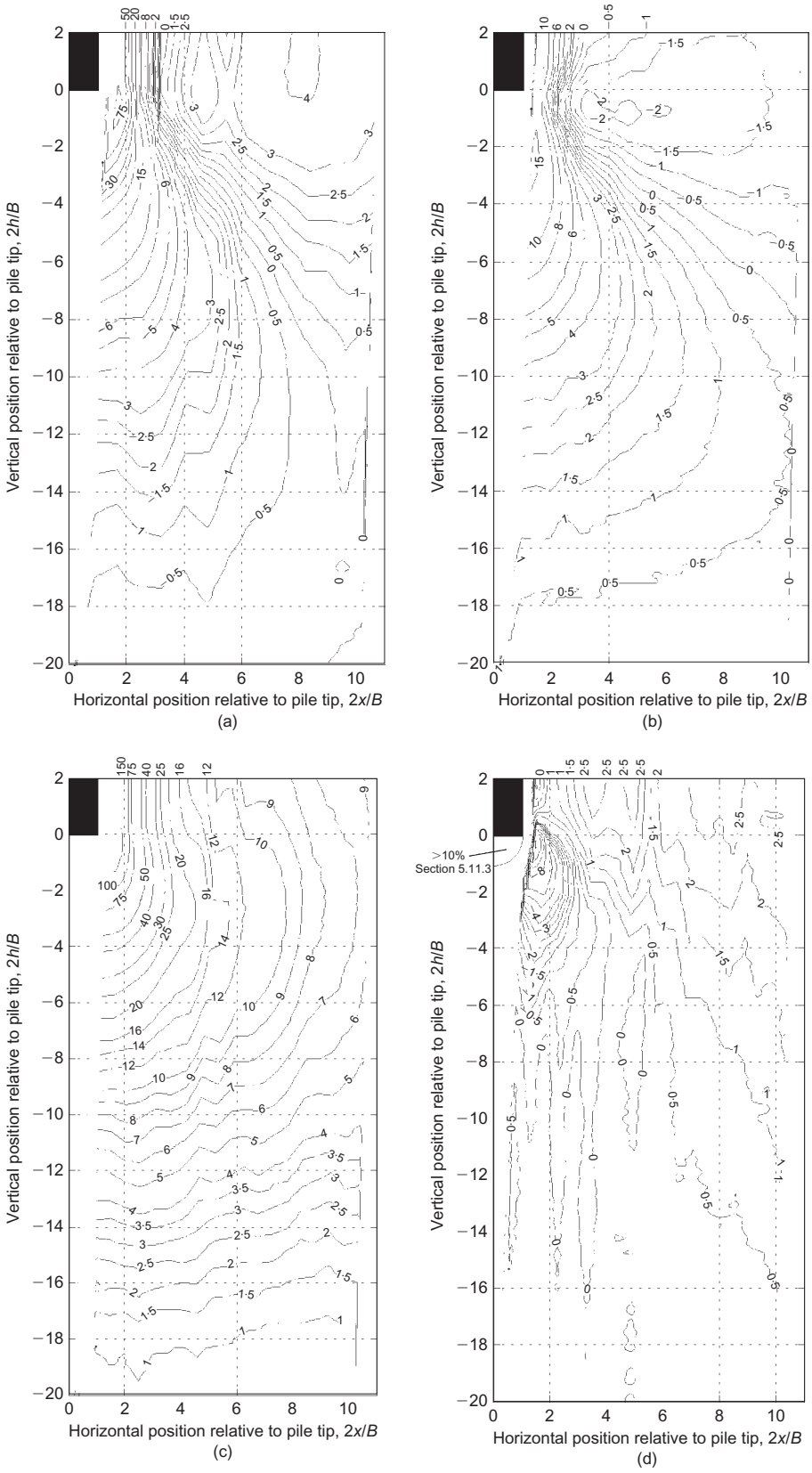

Fig. 18. Post-installation strain distribution, T4-LBS-34: (a) horizontal strain (%); (b) vertical strain (%); (c) maximum shear strain (%); (d) volumetric strain (%)

in the near field. As these values of strain are referred to the reference frame of the soil element, in zones of high rigid body rotation the horizontal and vertical strain axes do not coincide with the x–h axes of the figure.

Bulbs of high horizontal and vertical strain extend below and to the side of the pile in both DBS and LBS. In both cases the strain level adjacent to the pile is lower than below it. If installation is considered as the upward flow of soil past a stationary pile, then the strain path reversals can be seen as the soil flowing into and out from these bulbs of

high strain. The upper extent of the bulbs of vertical and horizontal strain is bounded by the contour of zero strain. Above this contour the initial strain probe has been entirely reversed, and the soil is now straining for the first time in the opposite sense to the original probe.

In contrast to the bulb-shaped distributions of vertical and horizontal strain, the zone of maximum shear strain does not significantly reduce in width as the soil flows past the pile tip. The high shear strain induced as the soil flows to the 55° strain reversal points (Fig. 16) is maintained as the soil moves past the pile.

Comparison of Figs 18 and 19 allows the influence of the ratio of chamber width to pile size to be examined. As there is good agreement between the shape and the absolute values of the contours of strain around each pile, the end wall boundary effect evidently has negligible influence on the kinematic behaviour close to the pile.

Figures 17 and 18 reveal differing volumetric behaviour in DBS and LBS. In DBS the zone of compression extends further below the pile. Adjacent to the pile shaft, monotonically decreasing compression with increasing offset is apparent in DBS. In LBS a zone of net dilation is evident around the pile shoulder and close to the pile shaft; a contour of zero volumetric strain is found at an offset of $2x/B = 1{\cdot}5$, with compression beyond. This variation of volumetric strain with offset from the pile shaft is discussed later, after observations of the volume change in the interface layer immediately adjacent to the pile have been presented.

COMPARISON WITH THEORETICAL SOLUTIONS

The penetration mechanism characterised by the strain paths shown in Figs 13 and 14 corresponds qualitatively with predictions based on the strain path method (SPM), originally proposed by Baligh (1985) and extended by others (Whittle & Baligh, 1988; Teh & Houlsby, 1991; Sagaseta *et al.*, 1997; Gill & Lehane, 2000; Yu *et al.*, 2000). Most published SPM solutions are limited to undrained penetration in axisymmetry, and so do not capture the volumetric behaviour associated with sand. However, the SPM captures the general trend of a gently increasing vertical and horizontal strain rate, followed by a sharp reversal as soil flows around the pile shoulder. In contrast, cavity expansion methods predict that each strain quantity will increase monotonically as the pile approaches (or the cavity is expanded), and therefore do not capture the strain history of the soil above the strain rate reversal lines shown in Fig. 16.

SOIL COMPRESSION DIRECTLY BELOW PILE

Measurement of the net horizontal displacement ratio for $2x_0/B = 1$ indicates the volumetric strain within the interface zone immediately adjacent to the pile (Fig. 10). The measured horizontal displacement ratio of $2\Delta x/B = 0{\cdot}8$ for $2x_0/B = 1$ implies a mean volumetric strain of 20% within the zone $2x_f/B < 1{\cdot}8$, indicating that the interface zone is significantly more dense than the very near field soil elements for which volumetric strain paths are shown in Fig. 15. Further evidence of densification close to the pile shaft is discussed below.

A highly compressed region of soil below the pile tip—hereafter referred to as a 'nose cone'—is visible during all tests on both DBS and LBS (Fig. 20(a)). Discrete slips of soil are observed to slide out from the nose cone and flow around the shaft of the pile. A central core of the nose cone is stationary relative to the pile tip, but the shoulders of the zone are not (Fig. 20(b)).

The nose cone from test T3-DBS-71 was sampled during the test post-mortem. The density was measured as 17·63 kN/m^3, indicating a specific volume of 1·53. This is equivalent to a volumetric compressive strain during the test of 32%. The stress-volume path of soil entering the nose cone is sketched on p'–v axes in Fig. 20(c). The mean pressure, p', is assumed to equal the measured value of q_b. The soil state lies below the CSL established by Klotz (2000), albeit for a different initial grading of DBS. A triaxial compression test at a similar mean pressure would result in less contraction, with the final state lying on the CSL. In the case of pile installation, the strain level is higher than is achieved during triaxial testing, which could lead to additional contraction. Luzzani & Coop (2002) made a similar observation from ring shear testing of DBS to a high strain level; a constant volume state was not reached.

The compressive strain on entering the nose cone could be partly balanced by dilation as the soil slips out from the nose cone, and shears around the shoulder of the pile into the interface zone, which is at a lower stress level. However, significant particle breakage occurs within the nose cone, changing the range of attainable voids ratios. The possible increase in volume as the soil leaves the high-stress zone below the pile tip and undergoes shear strain at low stress adjacent to the shaft was investigated by measuring the maximum voids ratio of the soil particles recovered by gently shaking the nose cone to break up the interlocked structure. The lowest achievable density was 15·15 kN/m^3, which corresponds to a specific volume of 1·78 ($e_{max} = 0{\cdot}78$). This value is significantly lower than both the maximum and minimum specific volumes of virgin DBS (Fig. 20(c)). This specific volume represents an upper limit on dilation of the broken soil. Even if the soil recovered to the minimum achievable density, a net volume compression of 21% would remain in the interface zone.

Full recovery to e_{max} as the soil rounds the pile shoulder and forms the interface layer would not occur, as the soil adjacent to the pile remains under load. An alternative stress–volume path would be to assume that the soil moves to a critical state. However, the CSL shown in Fig. 20(c) offers no p'–v state at a stress level lower than q_b yet at a density attainable by the broken soil; a new CSL must apply. The actual volumetric strain within the zone of soil adjacent to the shaft must lie between the value within the nose cone (32%) and the minimum attainable by the reconstituted soil (21%). Therefore the CSL for this heavily overconsolidated nose cone sand lies below the CSL for normally consolidated sand, in p'–v space.

Irrecoverable volume reduction was also observed for the LBS. The soil from the nose cone of test T4-LBS-34 was sampled in a disturbed state, and found to have a maximum specific volume of 1·61. This compares with 1·80 for the virgin LBS, and represents an irrecoverable volumetric strain of 10·5%. As with DBS, the actual volumetric strain adjacent to the pile must lie between this value and the greater (unknown) strain within the nose cone. These values of compression below the pile tip found from post-test sampling have been added to Figs 17 and 18 to supplement the volumetric strains calculated from image analysis.

These post-test index measurements indicate that the soil flowing around the pile tip and into the interface zone immediately adjacent to the pile shaft suffers significant irrecoverable volumetric compressive strain (>10%), accompanied by particle breakage. In contrast, Fig. 15 shows that dilation occurs slightly further from the pile tip. These two modes of volumetric behaviour are compared in Fig. 21, by considering the volume changes that are associated with the stress levels and shear strain encountered close to the pile tip.

Two streamlines of soil flow are shown in Fig. 21. Soil that flows through the nose cone and forms the interface

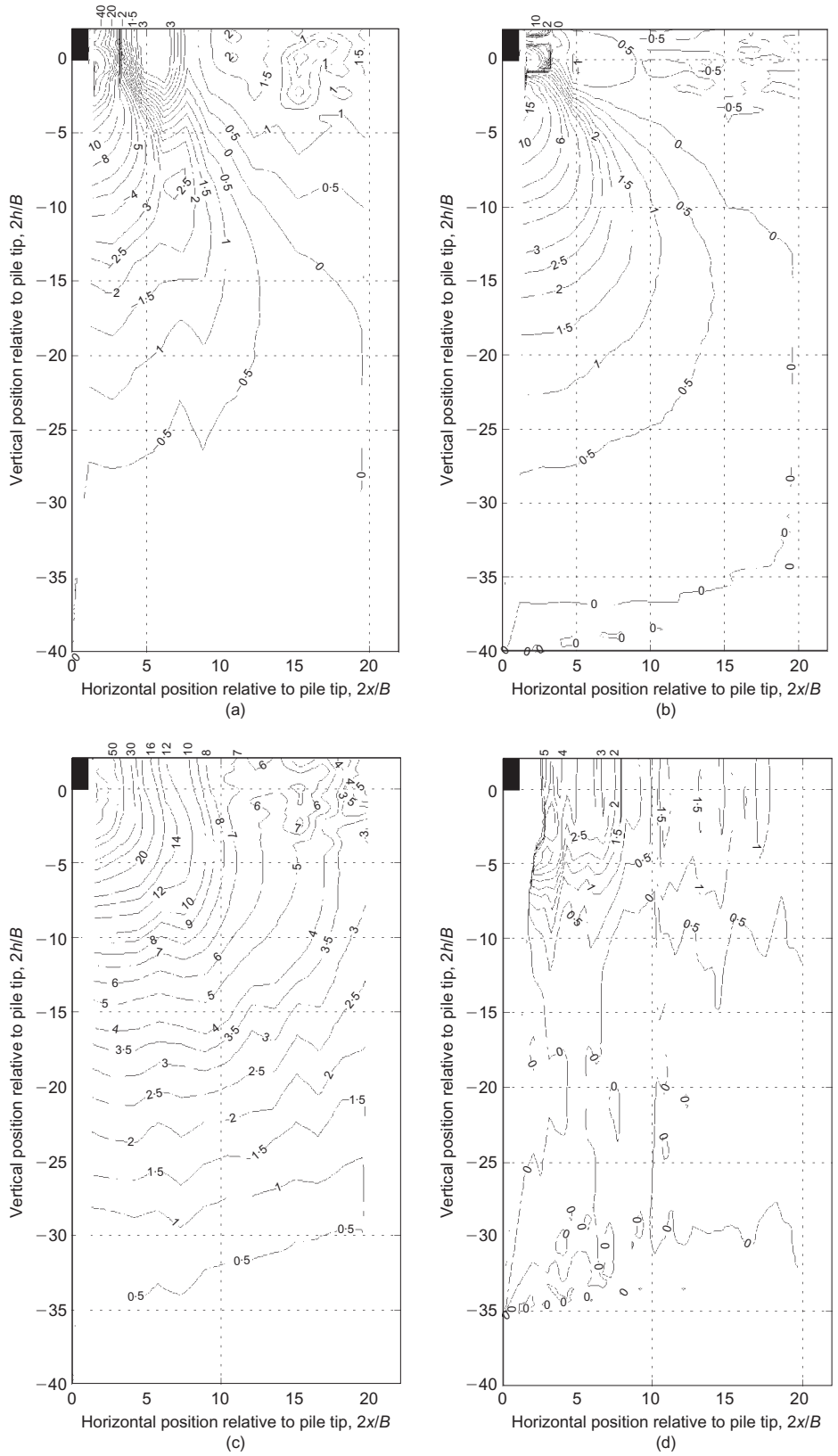

Fig. 19. Post-installation strain distribution, T8-DBS-46-narrow: (a) horizontal strain (%); (b) vertical strain (%); (c) maximum shear strain (%); (d) volumetric strain (%)

layer adjacent to the pile shaft follows streamline ABC. Soil in the very near field, for which PIV data are shown in Figs 17–19, follows streamline DEF. A zone of high stress corresponding to the photoelastic observations of Allersma (1988) during plane-strain pile penetration in crushed glass is shown below the pile tip.

Very high stress and very high shear strain are encountered along streamline AB, resulting in volume compression and significant particle breakage, as evident in photographs of the pile tip (Fig. 20(a)). This volume change is irrecoverable owing to particle breakage, as demonstrated by the index tests described previously. Therefore, as the soil

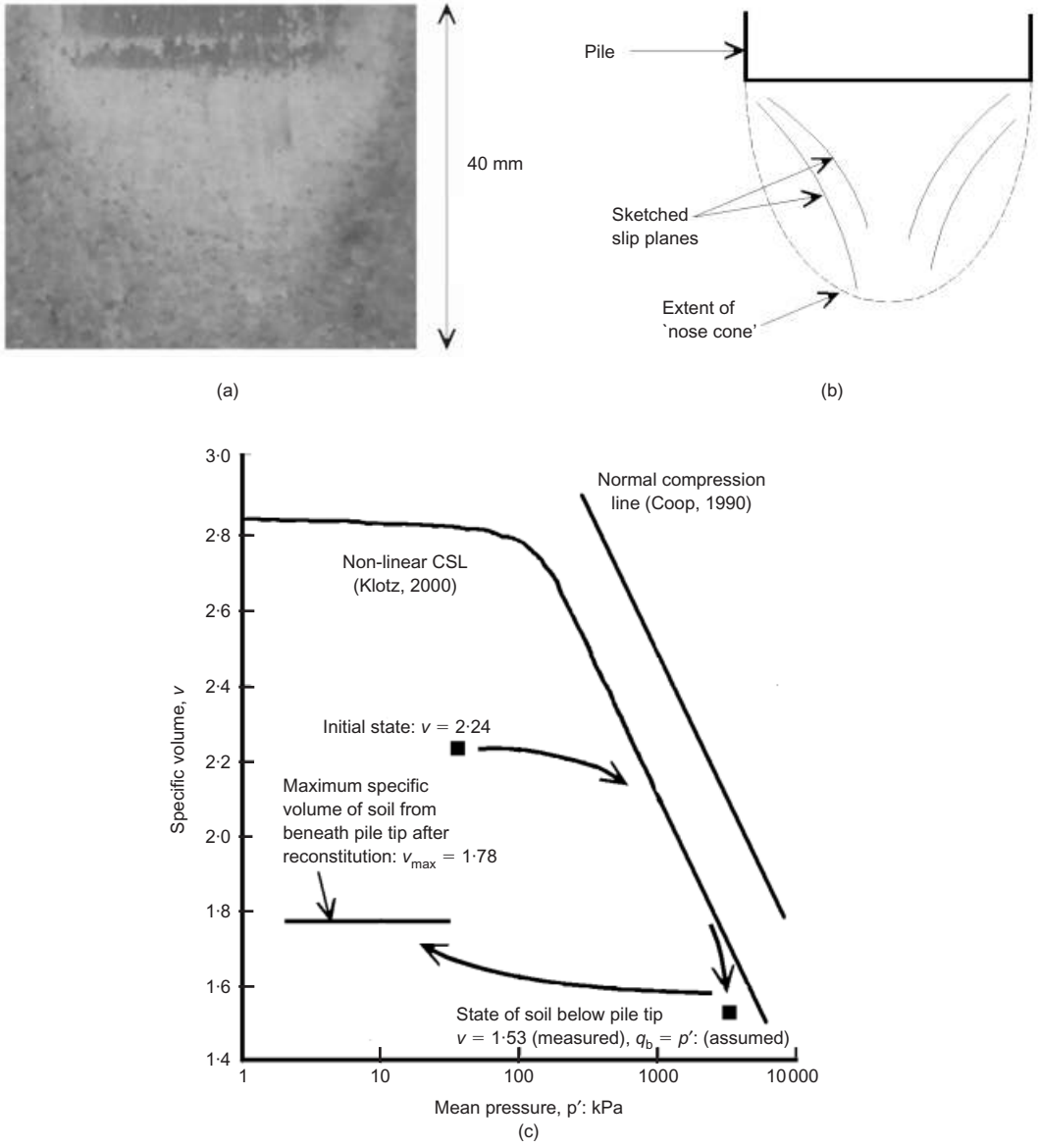

Fig. 20. Post-mortem sampling of soil below pile tip: (a) 'nose cone' of soil beneath pile tip (T4-LBS-34); (b) slip planes observed within nose cone; (c) stress–volume paths of soil beneath pile tip during test T3-DBS-71

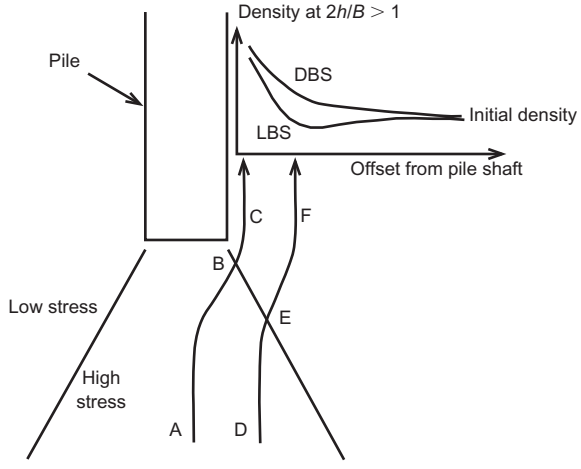

Fig. 21. Volumetric behaviour close to pile tip

progresses along the streamline BC, significant volume compression remains, creating a net increase in density.

Along streamline DE high stress and high shear strain are encountered, leading to contraction and some particle breakage. On leaving the zone of high stress, the soil is now heavily overconsolidated. Also, further shear strain is required for the soil to pass around the pile shoulder. The measured strain paths (Figs 13 and 14) show that the shear strain rate remains high within this zone, even though photoelastic analysis shows that the stress level has dropped. Critical state theory predicts that this overconsolidated soil will dilate when sheared along streamline EF. Such dilation is seen in Fig. 15. The slight volume compression along DE is more recoverable than the gross compression and particle breakage along AB.

The volumetric strain at the end of streamlines ABC (deduced from index tests) and DEF (deduced from image analysis) reveals the variation of density with offset from the pile shaft. This variation is shown schematically at the top

of Fig. 21. Adjacent to the pile shaft, the soil has become more dense, following irrecoverable volume change in the nose cone. In DBS the density decreases progressively away from the pile shaft. In LBS Fig. 18 indicates that this progressive decrease in density is interrupted by a local loose zone in the very near field caused by dilation close to the pile shoulder.

SOIL FLOW ADJACENT TO PILE SHAFT

The displacement trajectories shown in Fig. 8 have a 'tail', indicating movement of the soil towards the pile shaft after the tip has passed. A more detailed investigation of this behaviour was conducted using additional PIV meshes that were created in the zone of soil adjacent to the shaft and beyond the pile tip ($h > 0$). These meshes were used to observe the deformation within the soil after passage of the pile tip. As the soil close to the pile shaft undergoes only minimal deformation while $h > 0$, the PIV mesh could extend close to the pile surface. The closest column of PIV patches was located 4 mm from the pile shaft. Results are presented from tests T2-DBS-44 and T4-LBS-34.

Figure 22(a) shows the tip of the pile entering the field of view during test T2-DBS-44, with a row of PIV patches established adjacent to the pile shaft. Comparison with a subsequent image taken after 80 mm (2·5B) of further pene-

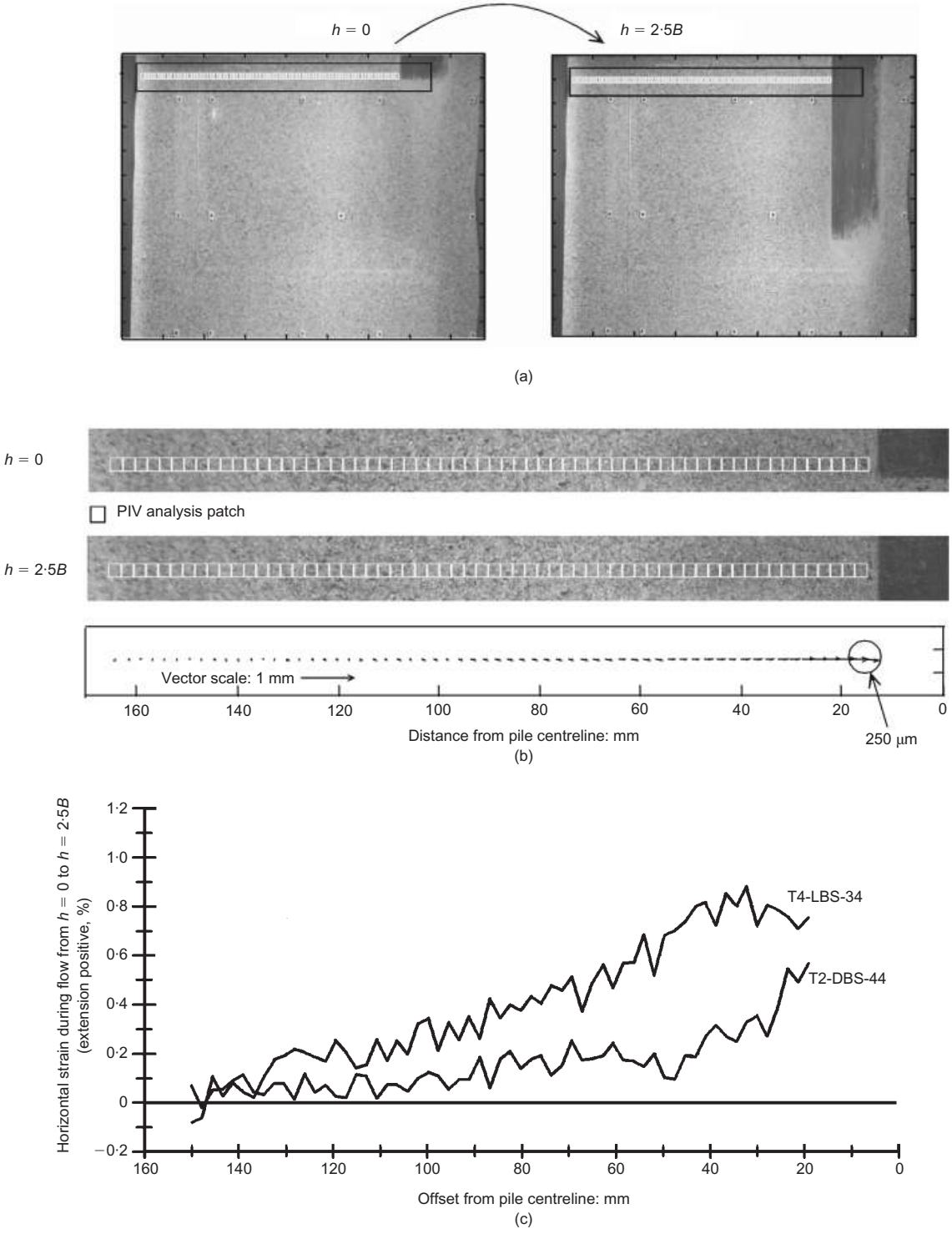

Fig. 22. Soil movement adjacent to pile shaft: (a) PIV patches established adjacent to pile shaft; (b) measured displacement vectors; (c) tests T2-DBS-44 and T4-LBS-34, horizontal unloading along a straight pile shaft

tration allowed the intervening soil movement to be measured. These vectors of displacement reveal that the soil is moving towards the pile shaft (Fig. 22(b)). The greatest vector (250 μm, 1·9 pixels) was measured at the patch closest to the pile (located 4 mm from the shaft). To eliminate the possibility that this observation was due to a non-vertical alignment of the pile, a set of patches on the opposite side of the pile were tracked. Similar vectors were obtained.

The horizontal strain profiles calculated from the displacement vectors measured adjacent to the pile during tests T2-DBS-44 and T4-LBS-34 are shown in Fig. 22(c). The soil adjacent to the pile unloads in horizontal extension as the pile advances and the interface zone contracts. Close-up photography during the test post-mortem revealed a 2–3 mm thick zone of fine broken particles adjacent to the pile shaft.

Figure 23 summarises the observed deformation mechanism adjacent to the model pile. This mechanism links the kinematic observation of a contractile interface zone to the degradation of shaft friction close to the pile tip. High horizontal stress is created as soil is compressed laterally along streamline XY. As the soil continues along streamline YZ the interface zone immediately adjacent to the pile (zone B in Fig. 24) contracts with continued shearing at the pile–soil interface. The stiff unloading response of the heavily overconsolidated soil in the far field is represented by a stiff spring (zone A). This spring is fixed in the far field and exerts horizontal stress on the pile shaft. As h increases, zone B contracts and this spring unloads, reducing the shaft friction on the pile.

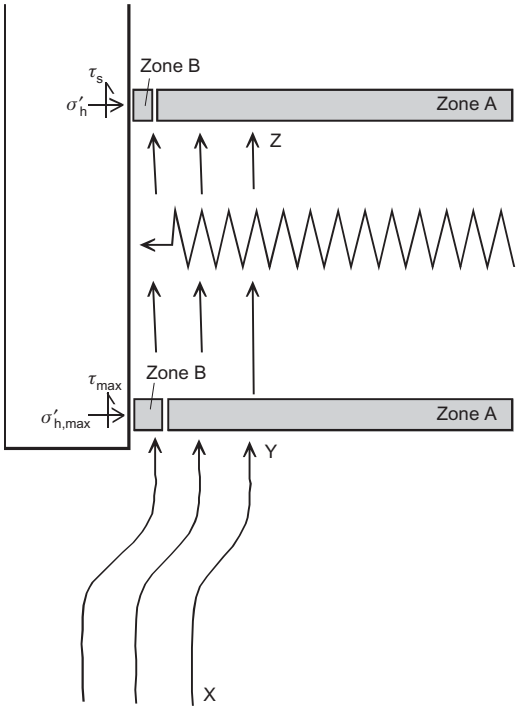

Fig. 23. Kinematics of friction fatigue close to the pile tip

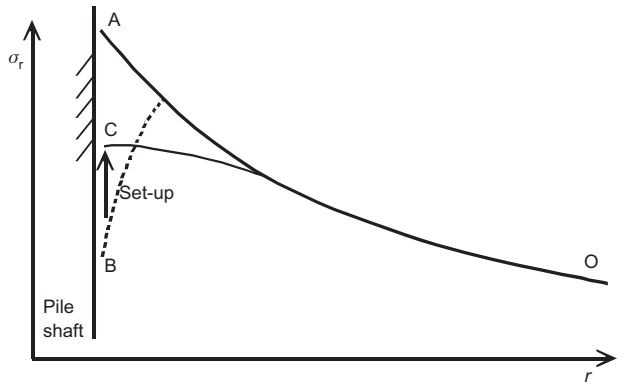

Fig. 24. Radial stress distribution due to interface contraction

SHAFT FRICTION DEGRADATION: 'FRICTION FATIGUE'

It has been widely observed in field and centrifuge model tests that the local shaft friction at a given soil horizon decreases as the pile tip penetrates further. This characteristic behaviour has been referred to as 'friction fatigue' (Heerema, 1980) or the 'h/R effect' (Bond & Jardine, 1991), and has been incorporated into recent design methods in an empirical manner (Randolph *et al.*, 1994; Jardine & Chow, 1996). This behaviour is captured by the mechanism shown in Fig. 24 arising from a contractile interface zone.

Conventional dynamic pile installation methods involve cyclic shearing at the pile–soil interface rather than the monotonic shearing applied in these tests. The mechanism of friction fatigue following interface contraction will be more significant under cyclic loading than under monotonic loading. It is widely reported from interface shear box testing that cycles of shear displacement lead to greater volume contraction than monotonic shearing (Al-Douri & Poulos, 1991; Tabucanon *et al.*, 1995; Dietz, 2000; DeJong *et al.*, 2003).

This link between cyclic shear displacement and reduced shaft friction is reported by Poulos *et al.* (1988). They note that the mean shaft friction measured in small-scale model pile tests after a given number of cycles decreases with increasing cyclic amplitude. Also, Dolwin *et al.* (1988) report a reduction in mean shaft friction with number of blows (and therefore displacement cycles) required for pile installation from CAPWAP analysis of driving records from long offshore piles in calcareous sand.

MECHANISM OF PILE SET-UP

The mechanism of interface contraction provides the initial conditions for set-up of displacement piles in sand, where 'set-up' refers to a time-related increase in shaft capacity, not related to pore pressure change. Immediately after passing the pile tip, the distribution of radial stress is as shown by the curve OA in Fig. 24, created as the soil is pushed outward during flow around the pile tip. As the interface zone contracts, cylindrical cavity collapse of the stiff overconsolidated soil close to the pile shaft leads to a sharp reduction in radial stress from the high value created during soil flow around the pile tip. As a result, the radial stress acting on the pile shaft (point B in Fig. 24) is lower than beyond the zone influenced by the cavity collapse. Over time, the high gradients in the stress field around the pile relax, creating the radial stress distribution shown as curve OC, which features an increase in the radial stress acting on the pile shaft and hence set-up.

This mechanism is similar to that proposed by Åstedt *et al.* (1992), in which high circumferential stresses, which initially 'arch' around the pile shaft, relax onto the pile surface over time, leading to an increase in shaft friction.

CONCLUSIONS

The results presented in this paper provide detailed experimental evidence of the penetration mechanism of a displacement pile. A novel image-based deformation measurement technique has been used to observe the displacement and

strain paths induced by the installation of a plane-strain model pile into a surcharged calibration chamber. The high precision offered by the measurement technique has allowed more detailed analysis of the penetration mechanism than has previously been possible.

A series of eight tests are reported, examining the influence of soil type, initial state, pile breadth and the use of a driving shoe. The displacement fields and strain paths during pile installation are found to be relatively independent of soil type, although greater compression and a smaller zone of influence are evident in carbonate sand than in silica sand. The shape of the strain path reveals high vertical compression below the pile tip, followed by horizontal compression as the soil element flows around the pile shoulder. This reversal of strain direction is in contrast to cavity expansion solutions, which predict monotonic strain paths. However, the key features of the penetration mechanism are captured by the strain path method.

The interface zone adjacent to the pile shaft comprised soil particles that had been broken while passing through the zone of high stress below the pile tip, leading to high irrecoverable volume reduction. This interface zone was observed to contract further while shearing along the pile–soil interface, indicating a mechanism for the degradation of shaft friction at a given soil horizon with increased pile penetration. This observed contraction has been linked to the influence of installation method on pile capacity and the possibility of time-related changes in shaft friction (set-up).

APPENDIX 1: STRAIN CALCULATION PROCEDURE

In order to calculate strain paths and element rotations the grid of PIV patches is divided into a network of triangular elements (Fig. 25). The strain and rotation of the element are calculated as follows.

The movement of each marker during a single displacement increment is used to construct the displacement gradient matrix, L, using shape functions (Zienkiewicz, 1967):

$$L = \begin{bmatrix} \frac{\partial u}{\partial X} & \frac{\partial u}{\partial Y} \\ \frac{\partial v}{\partial X} & \frac{\partial v}{\partial Y} \end{bmatrix} \tag{1}$$

The displacement gradient matrix is converted to the deformation gradient matrix, F, using

$$F = \begin{bmatrix} \frac{\partial x}{\partial X} & \frac{\partial x}{\partial Y} \\ \frac{\partial y}{\partial X} & \frac{\partial y}{\partial Y} \end{bmatrix} = L + I \tag{2}$$

where I is the identity matrix.

The deformation gradient matrix represents the transformation of a vector from undeformed coordinates, x_i, y_i to deformed coordinates, x_i', y_i' (Fig. 25):

$$\begin{pmatrix} x_i' \\ y_i' \end{pmatrix} = F \begin{pmatrix} x_i \\ y_i \end{pmatrix} \tag{3}$$

Polar decomposition allows the deformation gradient matrix to be divided into strain and rotation components, in order that individual components of deformation can be extracted (Chadwick, 1976; Belytschko *et al.*, 2000). The symmetric part of F is the stretch matrix, U, representing strain, with the skew-symmetric part, R, containing rotation. $(U)^2$ is known as the right Cauchy-Green strain matrix. R is antisymmetric, $R^{\mathrm{T}}R = I$, allowing F to be decomposed as follows:

$$U = (F^{\mathrm{T}}F)^{1/2} \tag{4}$$

$$R = FU^{-1} \tag{5}$$

The rotation matrix, R, has the form shown below in equation (6), allowing the rigid body rotation, θ, during the deformation described by F to be found. This rotation indicates the orientation of the material (soil) reference frame, *xy*, compared with the fixed (camera) reference frame, *XY*.

$$R = \begin{bmatrix} \cos\theta & -\sin\theta \\ \sin\theta & \cos\theta \end{bmatrix} \tag{6}$$

The Biot strain matrix, E^{Biot}, is found from the stretch matrix, U, using the following equation:

$$E^{\mathrm{Biot}} = U - I \tag{7}$$

The diagonal elements of E^{Biot} represent the elongation (change in length divided by original length) of line elements oriented with the x and y axes—that is, engineering linear strain:

$$\varepsilon_{\mathrm{eng},xy} = E_{11}^{\mathrm{Biot}} \tag{8}$$

$$\varepsilon_{\mathrm{eng},yy} = E_{22}^{\mathrm{Biot}} \tag{9}$$

The sum of the off-diagonal elements is equal to the engineering shear strain on the xy plane, γ_{xy}:

$$\gamma_{xy} = E_{12}^{\mathrm{Biot}} + E_{21}^{\mathrm{Biot}} \tag{10}$$

The eigenvalues of E^{Biot} are equal to the principal engineering strains, $\varepsilon_{\mathrm{eng,I}}$, $\varepsilon_{\mathrm{eng,II}}$, with the eigenvectors indicating the inclination of the principal strain directions to the xy axes.

Natural (logarithmic) strain is defined as the natural logarithm of the current length divided by the original length of a line element.

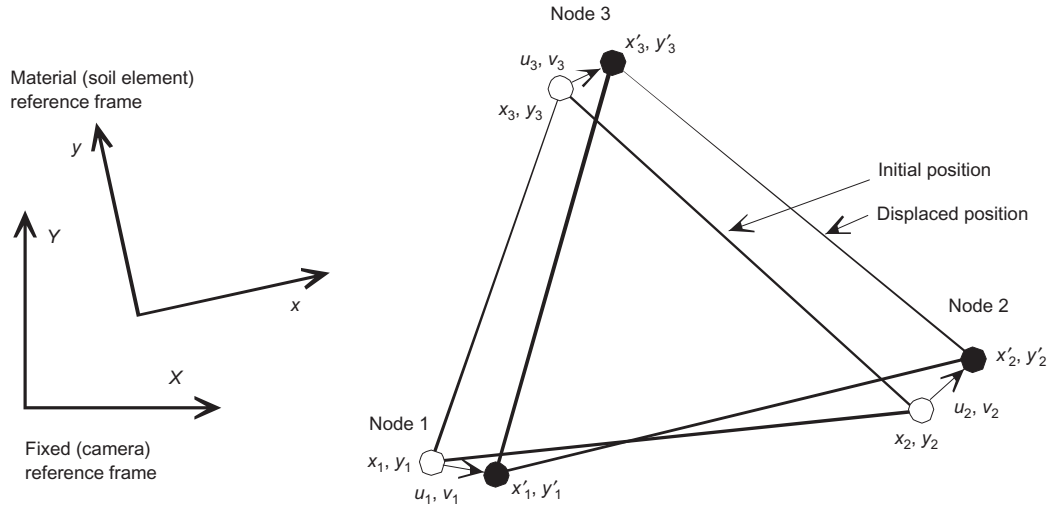

Fig. 25. Triangular element defined by three PIV patches

The natural strains in the x and y directions are found by taking the logarithm of the diagonal elements of U:

$$\varepsilon_{\log,xx} = \log_e(U_{11}) \quad (11)$$

$$\varepsilon_{\log,yy} = \log_e(U_{22}) \quad (12)$$

The engineering principal strain quantities can be converted to natural strain using the following equations:

$$\varepsilon_{\log,I} = \log_e(1 + \varepsilon_{eng,I}) \quad (13)$$

$$\varepsilon_{\log,II} = \log_e(1 + \varepsilon_{eng,II}) \quad (14)$$

To complete the set of natural strain quantities, maximum natural shear strain is defined as the difference between the natural principal strains:

$$\gamma_{\log,max} = \varepsilon_{\log,I} - \varepsilon_{\log,II} \quad (15)$$

REFERENCES

Airey, D. W., Randolph, M. F. & Hyden, A. M. (1988). The strength and stiffness of two calcareous sands. *Proc. Int. Conf. on Engng for Calcareous Sediments, Perth*, Vol. 1, pp. 43–50.

Al-Douri, R. H. & Poulos, H. G. (1991). Static and direct shear tests on carbonate sands. *ASTM Geotech. Test. J.* **15**, No. 2, 138–157.

Allersma, H. G. B. (1988). Photoelastic investigation of the stress distribution during penetration. *Proc. 2nd Eur. Symp. Penetration Testing, Amsterdam*, 411–418.

API (2000). *Recommended practice of planning, designing and constructing fixed offshore platforms: working stress design*, RP2A, 20th edn, pp. 59–61. Washington: American Petroleum Institute.

Åstedt, B., Weiner, L. & Holm, G. (1992). Increase in bearing capacity with time for friction piles in silt and sand. *Proceedings of Nordic Geotechnical Meeting*, pp. 411–416.

Atkinson, J. H., Richardson, D. & Stallebrass, S. E. (1990). Effect of recent stress history on the stiffness of overconsolidated soil. *Géotechnique* **40**, No. 4, 531–540.

Baligh, M. M. (1985). Strain path method. *ASCE J. Geotech. Engng* **111**, No. 9, 1108–1136.

Belytchko, E., Liu, W. K. & Moran, B. (2000). *Non-linear finite elements for continua and structures*. Chichester: Wiley.

Berezantzev, V. C., Kristoforov, V. & Golubkov, V. (1961). Load-bearing capacity and deformation of piled foundations. *Proc. 5th Int. Conf. Soil Mech. Fdn. Engng, Paris* **2**, 11–12.

Bolton, M. D., Gui, M. W., Garnier, J., Corte, J. F., Bagge, G., Laue, J. & Renzi, R. (1999). Centrifuge cone penetration tests in sand. *Géotechnique* **49**, No. 4, 543–552.

Bond, A. J. & Jardine, R. J. (1991). Effects of installing displacement piles in a high OCR clay. *Géotechnique* **41**, No. 3, 341–363.

Borghi, X., White, D. J., Bolton, M. D. & Springman, S. M. (2001). Empirical pile design based on CPT results: an explanation for the reduction of unit base resistance between CPTs and piles. *Proc. 5th Int. Conf. on Deep Foundation Practice, Singapore*, 125–132.

Bowman, E. T., Soga, K. & Drummond, W. (2001). Particle shape characterisation using Fourier descriptor analysis. *Géotechnique* **51**, No. 6, 545–554.

BSI (1990). *British Standard methods of tests for soils for civil engineering purposes*, BS 1377. Milton Keynes: British Standards Institution.

Bruno, D. (1999). *Dynamic and static load testing of driven piles in sand*. PhD thesis, University of Western Australia.

Budhu, M. (1979). *Simple shear deformation of sands*. PhD thesis, University of Cambridge.

Chadwick, P. (1976). *Continuum mechanics: concise theory and problems*. London: George Allen & Unwin.

Chong, F. (1988). Density changes of sand on cone penetration resistance. *Proc. 1st Symp. Penetration Testing, ISOPT-1*, **2**, 707–714. Rotterdam: Balkema.

Chow, F. C. (1997). *Investigations into the behaviour of displacement piles for offshore foundations*. PhD thesis, University of London (Imperial College).

Coop, M. R. (1990). The mechanics of uncemented carbonate sands. *Géotechnique* **40**, No. 4, 607–626.

Davidson, J. L., Mortensen, R. A. & Barreiro, D. (1981). Deformations in sand around a cone penetrometer tip. *Proc. 10th Int. Conf. Soil Mech. Fdn. Engng Stockholm* **2**, 467–470.

DeJong, J., Randolph, M. F. & White, D. J. (2003). Interface load transfer degradation during cyclic loading: a microscale investigation. *Soils Found.* **43**, No. 4, 81–93.

Dietz, M. S. (2000). *Developing an holistic understanding of interface friction using sand within the direct shear apparatus*. PhD thesis, University of Bristol.

Dolwin, J., Khorshid, M. S. & Van Goudoever, P. (1988). Evaluation of driven pile capacities: methods and results. *Proc. Int. Conf. Engng for Calcareous Sediments*, Perth, Vol. 2, pp. 409–428.

Gill, D. R. & Lehane, B. M. (2000). Extending the strain path analogy for modelling penetrometer installation. *Int. J. Numer. Anal. Methods Geomech.* **24**, 477–489.

Golightly, C. R. (1989). *Engineering properties of carbonate sands*. PhD thesis, Bradford University.

Golightly, C. R. & Hyde, A. F. L. (1988). Some fundamental properties of carbonate soils. *Proc. Int. Conf. Calcareous Sediments*, Vol. 1, pp. 69–78.

Heerema, E. P. (1980). Predicting pile driveability: heather as an illustration of the friction fatigue theory. *Ground Engng* **13**, 15–37.

Houlsby, G. T., Evans, K. M. & Sweeney, M. A. (1988). End bearing capacity of model piles in layered carbonate soils. *Proc. Int. Conf. on Engng for Calcareous Sediments, Perth,* Vol. 1, pp. 209–214.

Houlsby, G. T. & Hitchman, R. (1988). Calibration chamber tests of a cone penetrometer in sand. *Géotechnique* **38**, No. 1, 39–44.

Jardine, R. J. & Chow, F. C. (1996). *New design methods for offshore piles*, MTD Publication 96/103. London: Marine Technology Directorate.

Jardine, R. J., Symes, M. J. & Burland, J. B. (1984). The measurement of soil stiffness in the triaxial apparatus. *Géotechnique* **34**, No. 3, 323–340.

Jardine, R. J., Standing, J. R., Jardine, F. M., Bond, A. J. & Parker, E. (2001). Competition to assess the reliability of pile prediction methods. *Proc. 15th Int. Conf. Soil Mech. Geotech. Engng, Istanbul* **2**, 911–914.

Jovičič, V. & Coop, M. R. (1997). Stiffness of coarse-grained soils at small strains. *Géotechnique* **47**, No. 3, 545–561.

Klotz, E. U. (2000). *Influence of state on the capacity of driven piles in sand*. PhD thesis, City University, London.

Klotz, E. U. & Coop, M. R. (2001). An investigation of the effect of soil state on the capacity of driven piles in sands. *Géotechnique* **51**, No. 9, 733–751.

Kraft, L. M. (1990). Computing axial pile capacity in sands for offshore conditions. *Marine Geotech.* **9**, 61–72.

Lee, J. H. & Salgado, R. (1999). Determination of pile base resistance in sands. *ASCE J. Geotech. Geoenviron. Engng* **125**, No. 8, 673–683.

Lee, S. Y. (1989). *Centrifuge modelling of cone penetration testing in cohesionless soils*. PhD thesis, Cambridge University.

Lunne, T., Robertson, P. K. & Powell, J. J. M. (1997). *Cone penetration testing in geotechnical practice*. London: Blackie.

Luzzani, L. & Coop, M. R. (2002). On the relationship between particle breakage and the critical state of sands. *Soils Found.* **42**, No. 2, 71–82.

Mikasa, M. & Takada, N. (1973). Significance of centrifugal model tests in soil mechanics. *Proc. 8th Int. Conf. Soil Mech. Fdn. Engng, Moscow*, 273–278.

Poulos, H. G., Randolph, M. F. & Semple, R. M. (1988). Evaluation of pile friction from conductor tests. *Proc. Int. Conf. Calcareous Sediments*, *Perth*, Vol. 2, pp. 599–605.

Randolph, M. F., Dolwin, J. & Beck, R. (1994). Design of driven piles in sand. *Géotechnique* **44**, No. 3, 427–448.

Robinsky, E. I. & Morrison, C. F. (1964). Sand displacement and compaction around model friction piles. *Can. Geotech. J.* **1**, No. 2, 81–93.

Sagaseta, C., Whittle, A. J. & Santagata, M. (1997). Deformation analysis of shallow penetration in clay. *Int. J. Numer. Anal. Methods Geomech.* **21**, No. 10, 687–719.

Salgado, R., Mitchell, J. K. & Jamiolkowski, M. (1997). Cavity expansion and penetration resistance in sand. *ASCE J. Geotech. Geoenviron. Engng* **123**, No. 4, 344–354.

Schnaid, F. (1990). *A study of the cone-pressuremeter test in sand*. DPhil thesis, Oxford University.

Sentenac, P., Lynch, R. J. & Bolton, M. D. (2001). Measurement of the side-wall boundary effect in soil columns using fibre-optics sensing. *Int. J. Physical Modelling in Geotechnics* **1**, No. 4, 35–41.

Stroud, M. A. (1971). *Sand at low stress levels in the simple shear apparatus*. PhD thesis, Cambridge University.

Tabucanon, J. T., Airey, D. W. & Poulos, H. G. (1995). Pile skin friction in sands from constant normal stiffness tests. *ASTM Geotech. Test. J.* **18**, No. 3, 350–364.

Tan, F. S. C. (1990). *Centrifuge and theoretical modelling of conical footings on sand*. PhD thesis, Cambridge University.

Teh, C. I. & Houlsby, G. T. (1991). Analytical study of the cone penetration test in clay. *Géotechnique* **41**, No. 1, 17–34.

Tejchman, A. & Gwizdala, K. (1979). Analysis of safety factors of bearing capacity for large diameter piles. *Proc. Eur. Conf. Soil Mech. Fdn Engng, Brighton* **1**, 293–296.

White, D. J. (2002). *An investigation into the behaviour of pressed-in piles*. PhD thesis, University of Cambridge.

White, D. J., Take, W. A. & Bolton, M. D. (2003). Soil deformation measurement using particle image velocimetry (PIV) and photogammetry. *Géotechnique* **53**, No. 7, 619–631.

White, D. J. & Bolton, M. D. (2004). A review of field measurements of CPT and pile base resistance. *Proc. Instn Civ. Engrs, Geotech. Engng,* forthcoming.

Whittle, A. J. & Baligh, M. M. (1988). *The behaviour of piles supporting tension leg platforms*, Final MIT Sea Grant & Joint Industry Consortium Report. Department of Civil Engineering, Massachusetts Institute of Technology.

Winterkorn, A. F. & Fang, S. Y. (1975). *Foundation engineering handbook*. New York: Van Nostrand Reinhold.

Yasufuku, N. & Hyde, A. F. L. (1995). Pile end-bearing capacity in crushable sands. *Géotechnique* **45**, No. 4, 663–676.

Yu, H. S., Herrman, L. R. & Boulanger, R. W. (2000). Analysis of steady cone penetration in clay. *ASCE J. Geotech. Geoenviron. Engng* **126**, No. 7, 594–605.

Zienkiewicz, O. C. (1967). *The finite element method in structural and continuum mechanics*. London: McGraw-Hill.